

# Direct observation of angular momentum transfer among crystal lattice modes

Olga Minakova<sup>1</sup>, Carolina Paiva<sup>2</sup>, Maximilian Frenzel<sup>1</sup>,  
Michael S. Spencer<sup>1</sup>, Joanna M. Urban<sup>1</sup>, Christoph Ringkamp<sup>3,4</sup>,  
Martin Wolf<sup>1</sup>, Gregor Mussler<sup>3,4</sup>, Dominik M. Juraschek<sup>2,5</sup>,  
Sebastian F. Maehrlein<sup>1,6,7†</sup>

<sup>1</sup>Fritz Haber Institute of the Max Planck Society, Department of  
Physical Chemistry, Berlin, Germany.

<sup>2</sup>Tel Aviv University, School of Physics and Astronomy, Tel Aviv, Israel.

<sup>3</sup>Peter Grünberg Institut (PGI-9), Forschungszentrum Jülich, Jülich,  
Germany.

<sup>4</sup>JARA-Fundamentals of Future Information Technology, Jülich-Aachen  
Research Alliance, Forschungszentrum Jülich GmbH and RWTH  
Aachen University, Germany.

<sup>5</sup>Eindhoven University of Technology, Department of Applied Physics  
and Science Education, Eindhoven, Netherlands.

<sup>6</sup>Helmholtz-Zentrum Dresden-Rossendorf, Institute of Radiation  
Physics, Dresden, Germany.

<sup>7</sup>Dresden University of Technology, Institute of Applied Physics,  
Dresden, Germany.

†Email: s.maehrlein@hzdr.de

## Abstract

The discrete rotational symmetry of crystals leads to the conservation of quantized angular momentum in solids. While the exchange of energy and linear momentum between lattice vibrations (phonons) via anharmonic coupling is a cornerstone of solid-state physics, conservation and transfer of angular momentum within the lattice remains a postulate. Recently, phonon angular momentum, often in the form of chiral phonons [1–3], has been linked to giant magnetic fields [4], thermal Hall conductivity [5], dynamical multiferroicity [6], ultrafast demagnetization [7, 8], or magnetic switching [9]. However, the inherent process of phonon to phonon angular momentum transfer, fundamentally required

to reach any magnetization equilibrium [8, 10] and imperative for all spin relaxation phenomena in solids [11, 12], remains elusive.

Here, we demonstrate the coherent transfer of angular momentum from one lattice mode to another by establishing helical nonlinear phononics. We directly observe rotational phonon-phonon Umklapp scattering dictated by pseudo angular momentum conservation and the threefold rotational symmetry of the topological insulator bismuth selenide. We identify nonlinear phonon-phonon coupling as an angular momentum transfer channel, confirmed by our ab-initio calculations. Besides bearing universal implications for angular momentum dissipation abundant in nature [10, 12, 13], our work actively reverses the natural flow, leading to the nonlinear upconversion of lattice angular momentum. We thus open the field of helical and chiral nonlinear phononics, representing a selective handle for ultrafast control of spins, topology and chiral quasi-particles.

Fundamental physics is dictated by symmetry principles, linking conservation laws to time, space translation, and rotational invariance. In crystalline solids, discrete translational symmetry enforces the conservation of pseudo linear momentum, forming the basis of band structure theory and modern semiconductor-based technology. Likewise, quantized vibrations of the crystalline lattice must conserve energy and linear momentum during their interactions. Such energy and momentum relaxation through phonon-phonon scattering is required to establish equilibrium states of condensed matter. However, demagnetization - like all spin relaxation phenomena - additionally requires the dissipation of angular momentum to achieve equilibrium. While energy relaxation is established to follow pathways of anharmonic phonon-phonon coupling [14], transferring energy from optical to lower frequency acoustic modes and eventually becoming heat, the relaxation of angular momentum among lattice modes is commonly just assumed [13, 15]. Since the discovery of the Einstein - de Haas effect [10], it has been recognized that spin angular momentum must eventually transfer to the lattice as a rigid-body rotation, bridging quantum spin dynamics with classical mechanical angular momentum. However, how this transfer happens after the initial spin-lattice coupling [7, 8, 11] remains largely a black box to date.

Contemporary studies actively employ phonons for ultrafast control of material properties, as evidenced by signatures of light-induced superconductivity [16–18], ferromagnetism [19, 20] and ferroelectricity [21], thereby controlling collective phases of matter. Recently, researchers also utilized chiral or circularly polarized phonons, broadly classified as axial phonons [22], to harness their transient magnetic fields [4, 23–25] for magnetic switching [9] or dynamic multiferroicity [6]. Nevertheless, the corresponding phonon trajectories, as a direct measure of phonon angular momentum, could not be assessed in these studies and remain debated to explain the observed magnetic effects [26].

To achieve a net circular polarization of a doubly degenerate phonon mode near the  $\Gamma$ -point (long-wavelength limit), its orthogonal components need to be coherently driven with a phase delay of  $\pi/2$ . For IR-active  $E_u$  modes, this can be achieved by a circularly polarized laser pulse in the terahertz (THz) spectral domain, where the resonant (linear) coupling between the THz electric field and phonon's electric dipole directly imprints the helicity of light onto the phonon mode. Yet, the resulting phonon angular momentum has only been inferred from secondary effects, such as phonon magnetic fields [6, 9] or THz field-induced second harmonic generation [4]. For Raman-active modes, nevertheless, the lattice trajectory can be controlled and directly observed by all-optical experiments that utilize stimulated Raman scattering techniques [27]. In all these examples, angular momentum is transferred from the light field to the lattice mode, and then potentially further to spin states, which can be conveniently detected by magneto-optic measurements. However, tracing the consecutive flow of angular momentum from the initially excited phonon to other lattice modes has remained elusive and represents a huge gap in our understanding of ultrafast demagnetization and other spin-related phenomena since the pioneering experiments by Einstein, de Haas [10] and Barnett [28].

Here, we provide experimental evidence for angular momentum  $l_{\text{ph}}$  transfer between lattice modes by a coherent three-phonon scattering process, as sketched in Fig. 1a. Ionic Raman scattering, permitted by the lowest order anharmonic lattice potential, couples two quanta of IR-active phonons to a Raman-active phonon via  $(Q^{\text{IR}})^2 Q^{\text{R}}$ , where  $Q^{\text{IR}}$  and  $Q^{\text{R}}$  are the amplitudes of the IR- and Raman-active modes, respectively. The topological insulator  $\text{Bi}_2\text{Se}_3$  provides an ideal material platform to coherently drive a three-phonon scattering process of axial phonons: Due to its inversion symmetry,  $\text{Bi}_2\text{Se}_3$  accommodates either purely Raman- or IR-active doubly degenerate phonons in the  $a$ - $b$  plane parallel to the surface. At room temperature, an IR-active  $E_u$  mode at 2.0 THz dominates the THz absorption (see Extended Data Fig. 1). A Raman-active  $E_g$  mode at 4.0 THz is anharmonically coupled to this 2 THz mode [29], fulfilling the double-frequency resonance condition  $2\Omega^{\text{IR}} = \Omega^{\text{R}}$  for sum-frequency ionic Raman scattering [30, 31].

As shown in the experimental concept, sketched in Fig. 1b, we first resonantly excite a circularly polarized  $E_u$  mode. In contrast to recent pioneering works [4, 6, 9] employing such axial IR-phonons, we are not looking at the magneto-optic effects to study the angular momentum transfer to the spin system, instead we follow the trajectory of the coupled  $E_g$  mode via the non-magnetic THz-induced Kerr effect (TKE) [32, 33]. As both conservation of energy  $2\hbar\Omega^{\text{IR}} = \hbar\Omega^{\text{R}}$  and linear momentum  $2\hbar k^{\text{IR}} = \hbar k^{\text{R}} \approx 0$  (all  $\Gamma$ -modes) are perfectly fulfilled in this nonlinear process, we can study the isolated dynamics of angular momentum transfer and its conservation. By this experimental concept, we witness a helicity switch from one mode to the other, corresponding to the conservation of pseudo angular momentum (PAM) by a nonlinear phononic analogue to a rotational Umklapp process [34].

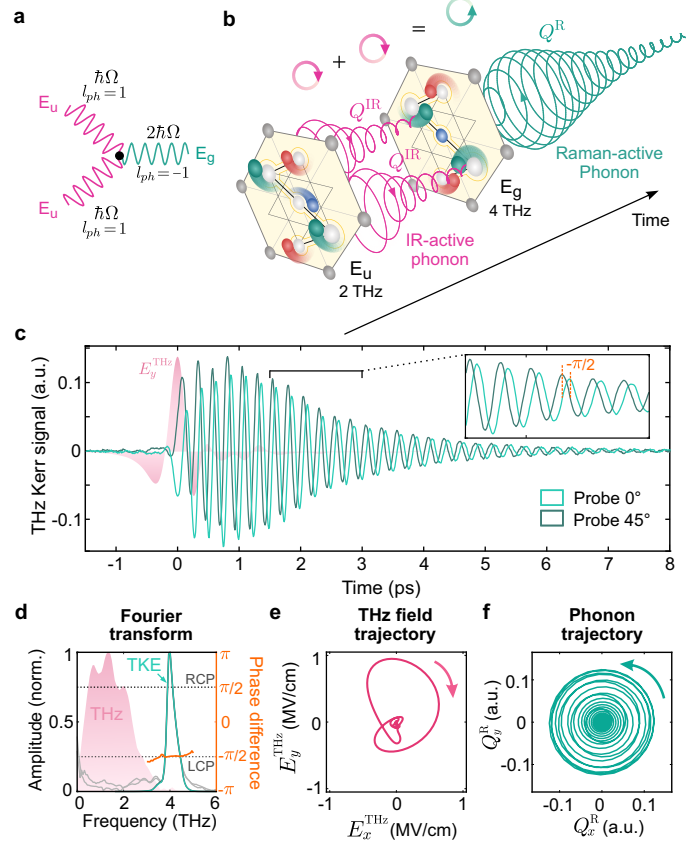


**Fig. 1 Phonon-phonon angular momentum transfer in bismuth selenide.** **a**, Investigated three-phonon scattering process: annihilation of two  $E_u$  phonons by one  $E_g$  phonon must conserve energy, (pseudo) linear momentum and pseudo angular momentum. **b**, Experimental concept: A coherent axial  $E_u$  mode (red) at 2 THz nonlinearly transfers energy and momentum to the axial  $E_g$  mode (green) at 4 THz with opposite helicity in Bi<sub>2</sub>Se<sub>3</sub>. **c**, THz-induced Kerr effect (TKE) in Bi<sub>2</sub>Se<sub>3</sub> (green) under right-handed circularly polarized THz excitation (red projection) for two linear probe pulse polarizations (0° and 45°), measuring two orthogonal  $E_g$  phonon components. Inset: zoom into time domain traces. **d**, Fourier transforms unveil equal amplitudes (green), but perfect  $-\pi/2$  phase difference (orange) of the  $E_g$  phonon projections in **c**, clearly outside the excitation spectrum (red shade). **e**, Trajectory of the excitation pulse's THz electric field vector. **f**,  $E_g$  phonon trajectory obtained by Fourier-filtered TKE signal from **c** unveils opposite helicity of the THz field in **e**.

## Results

We resonantly drive the  $E_u$  mode of a Bi<sub>2</sub>Se<sub>3</sub> single crystal epilayer (15 nm thickness), grown by molecular beam epitaxy on Al<sub>2</sub>O<sub>3</sub> (see Methods), by circularly polarized single-cycle THz pulses with peak fields exceeding 1.5 MV/cm (see Fig. 1c, red shade). We consecutively sample the transient birefringence induced by the oscillating coherent phonon with a sub-cycle (and thus phase-resolved precision) 20 fs probe pulse at 790 nm wavelength (see Methods). This all-optical measurement of coherent phonons

via the TKE is a time-domain probing scheme and selectively sensitive to Raman-active modes [32, 33]. With linear probe pulse polarizations at  $45^\circ$  and  $0^\circ$  with respect to an arbitrary lab frame, we observe a strong TKE signal dominated by a long-lived oscillatory signal as shown in Fig. 1c. Its Fourier transform in Fig. 1d, unveils a single dominant oscillation at 4.0 THz, exactly at the  $E_g$  mode's resonance [29]. Strikingly, this Raman-active phonon lies clearly outside the THz excitation spectrum (red area in Fig. 1d) and thus must be nonlinearly excited either by the absorption of two photons [35] or two coherent phonons [29–31], as confirmed by the quadratic field dependence in Extended Data Fig. 2b-e. Due to its lack of Raman activity, the  $E_u$  mode is not observed by the TKE, but instead by linear THz absorption (see Extended Data Fig. 1), in full agreement with the mutual exclusion principle in the centrosymmetric  $\text{Bi}_2\text{Se}_3$  crystal.

By measuring the probe polarization dependence of the phonon amplitude in Extended Data Fig. 3c, we show that the two orthogonal projections  $Q_x^R$  and  $Q_y^R$  can be separately measured by a  $45^\circ$  and  $0^\circ$  linear probe polarization, in full agreement with the two  $E_g$ -symmetry Raman tensors [36]

$$\mathbf{R}_x = \begin{pmatrix} c & 0 \\ 0 & -c \end{pmatrix}, \quad \mathbf{R}_y = \begin{pmatrix} 0 & -c \\ -c & 0 \end{pmatrix} \quad (1)$$

in the  $D_{3d}$  point group, respectively (see Methods). We can thus trace the complete two dimensional (2D) vibrational trajectory of the  $E_g$  mode in analogy to the seminal work employing double pulse impulsive stimulated Raman scattering [27]. By implementing polarization-resolved electro-optic sampling in  $\alpha$ -quartz [37], we precisely measure the full spatio-temporal trajectory of the THz electric field vector, tracing a right-handed helicity in Fig. 1e. In the TKE signals in Fig. 1c, very similar oscillations are found at  $45^\circ$  and  $0^\circ$  probe polarization, respectively corresponding to the two orthogonal  $E_g$  components  $Q_x^R$  and  $Q_y^R$  with identical amplitude spectra in Fig 1d. Both, the time domain inset in Fig. 1c and the complex Fourier transforms in Fig 1d, unambiguously unveil a phase difference of exactly  $-\pi/2$  between the orthogonal  $Q_x^R$  and  $Q_y^R$  components. Therefore, we here demonstrate the first THz-driven preparation and simultaneous measurement of a coherent phonon angular momentum state, often termed axial phonon or chiral phonon. This becomes directly evident from the 2D lattice trajectory in Fig. 1f, which strikingly reveals an opposite helicity compared to the driving field in Fig. 1e.

For systematic investigation of the phonon angular momentum transfer, we turn to tailored helical THz driving fields. By transformation of the exact THz field trajectories in Fig. 2a from time- into frequency domain, and from a linear  $(E_x, E_y)$  basis into a circular  $(E_{|R\rangle}, E_{|L\rangle})$  basis in Fig. 2b, we follow the complex evolution of the single cycle's helicity state across its broad spectrum. With this information, we customized a y-cut quartz waveplate plate (thickness 700  $\mu\text{m}$ ) to provide a pure right-hand (RCP) or left-hand circularly polarized (LCP) THz helicity state at 2 THz (see Figure 2b). The three distinct fields with net helicity  $l_s = -1, 0, 1$  at 2 THz in Fig. 2a, are then used to coherently drive the IR-active  $E_u$  phonon with a prescribed angular momentum state. By comparison of the resulting  $E_g$  phonon trajectories in Fig. 2c, we find an opposite phonon helicity compared to the THz driving field in Fig. 2a. Transforming also the

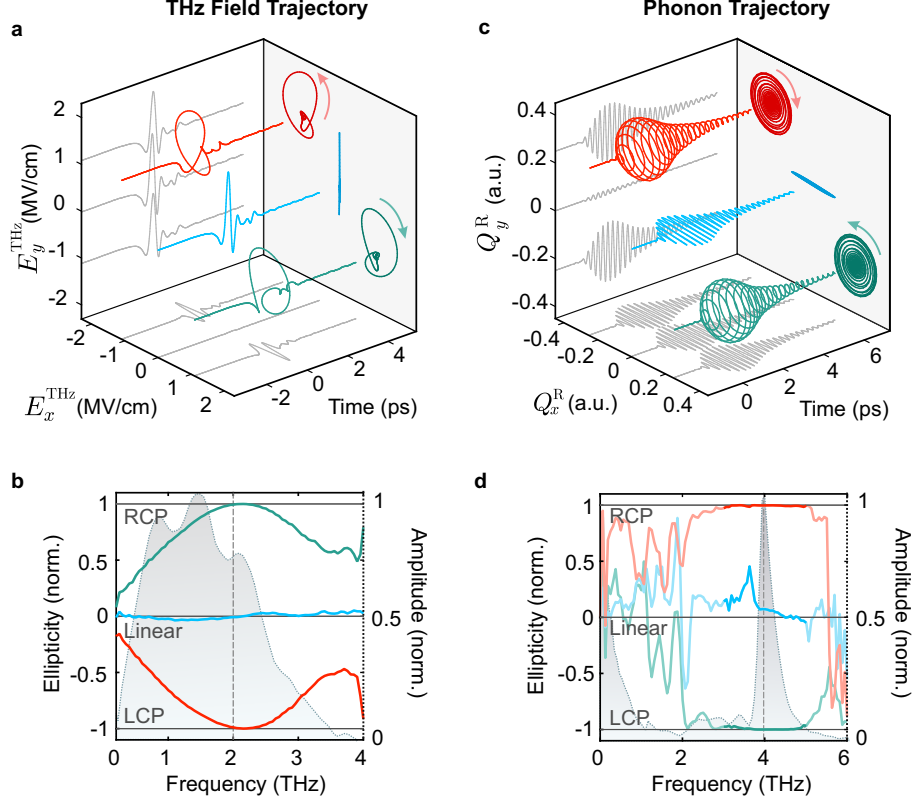


**Fig. 2 THz field and phonon trajectories and their helicity states.** **a**, Polarization-resolved EOS of the THz excitation electric fields tailored by a 700  $\mu\text{m}$ -thick  $y$ -cut quartz plate at three different azimuthal orientations. **b**, Frequency-decomposed ellipticity (colored lines) and amplitude (shaded area) of the excitation fields in **a**, calculated from the Stokes parameter  $S_3$  of the THz field's Fourier transform. At around 2 THz, the THz pump pulses exhibit well-defined linear (blue), right-circular (green), and left-circular (red) polarizations. **c**, Measured  $E_g$  phonon trajectories for each THz polarization state from **a**. **d**, Corresponding ellipticity decompositions of the TKE signals (colored lines) and Fourier filtered  $E_g$  trajectories in **c**. (darker colors). The  $E_g$  phonon at 4 THz shows full helicity reversal with respect to the THz electric field at 2 THz. The shaded area represents the TKE spectral amplitudes.

phonon trajectories into frequency domain and circular basis, the  $E_g$  phonons' Stokes vectors  $S_3(\Omega) = (|Q_{|R}^R(\Omega)|^2 - |Q_{|L}^R(\Omega)|^2)/Q^2$  unveil an extremely pure helicity of two opposite angular momentum states across the full phonon bandwidth. Accordingly, we find a helicity switch: For the excitation with a RCP (LCP) field at 2 THz, the Raman-active phonon at 4 THz possesses a perfect LCP (RCP) and thus opposite helicity (arrows in Figs. 2a,c). This phonon helicity reversal cannot be rationalized by probing effects, nor by a helicity switch of a Raman photon scattered by a chiral phonon [2] (see Methods).

Let us briefly summarize: First, we demonstrated the preparation and direct observation of a coherent state of phonon angular momentum by a THz-driven nonlinear

mechanism. Second, we find a helicity switch of the  $E_g$  mode compared to the circular driving field and to the presumably circularly polarized IR-active  $E_u$  mode. In the following, we will address two arising questions: What is the nonlinear excitation mechanism of the observed phonon angular momentum? And how is it conserved leading to the switched helicity?

Generally, the purely Raman-active  $E_g$  mode can be driven by a nonlinear photonic or nonlinear phononic pathway [30, 35, 38] sketched in Fig. 3a. In the photonic case, pairs of photons within the broad THz excitation spectrum excite the  $E_g$  mode via their sum-frequency polarization [35]. For the nonlinear phononic coupling, the initially driven IR-active  $E_u$  phonon couples via an  $(Q^{\text{IR}})^2 Q^{\text{R}}$  anharmonic term in the lattice potential  $V(Q^{\text{IR}}, Q^{\text{R}})$  to the Raman-active mode, known as sum-frequency ionic Raman scattering [30]. In the photonic case, the driving force for the  $E_g$  mode is given by  $\mathbf{E} \mathbf{R}_x \mathbf{E}$  and  $\mathbf{E} \mathbf{R}_y \mathbf{E}$  and is thus proportional to  $E_x^2 - E_y^2$  and  $-2E_x E_y$  for the  $Q_x^{\text{R}}$  and  $Q_y^{\text{R}}$  component, respectively. In the  $D_{3d}$  point group, to which  $\text{Bi}_2\text{Se}_3$  belongs, the lowest-order anharmonic lattice potential that couples the modes of interest is  $V(\mathbf{Q}^{\text{IR}}, \mathbf{Q}^{\text{R}}) = c[(Q_x^{\text{IR}})^2 - (Q_y^{\text{IR}})^2]Q_x^{\text{R}} - 2cQ_x^{\text{IR}}Q_y^{\text{IR}}Q_y^{\text{R}} + O(Q^4)$ , where  $c$  is the anharmonic coupling constant determined by our DFT calculations (see Methods). Its derivative with respect to the Raman-active phonon coordinate  $\partial V/\partial \mathbf{Q}$  yields the ionic driving forces proportional to  $F_x = c[(Q_x^{\text{IR}})^2 - (Q_y^{\text{IR}})^2]$  and  $F_y = -2cQ_x^{\text{IR}}Q_y^{\text{IR}}$ , respectively. Therefore, both driving mechanisms obey the same symmetry dictated by the  $D_{3d}$  point group. One way to distinguish these two pathways is by their respective driving force dynamics, leading to different phonon rise times when solving the respective  $\mathbf{Q}^{\text{R}}$  equations of motion, as shown for  $Q_x^{\text{R}}$  in Fig. 3b. We find that the rise time of the experimental trace, matching the  $E_u$  lifetime as measured by THz transmission in Extended Data Fig. 2, is only reproduced by the phononic driving force, pinpointing the excited IR-active  $E_u$  phonon as the primary driving force of the Raman-active phonon.

To quantify the contribution of the nonlinear phonon-phonon angular momentum transfer, we calculate the total angular momentum  $L^{\text{R}}$  of the excited  $E_g$  phonon from the photonic versus the phononic driving pathway. We compute all involved light-matter coupling parameters, Raman tensors, and anharmonic coupling parameters  $c$  up to the 4th order using density functional theory (see Methods). Strikingly, our ab-initio model, predicts a 3 order-of-magnitude increase in angular momentum transfer from the IR-active  $E_u$  mode to the  $E_g$  mode compared to the direct driving of the  $E_g$  mode via the photonic excitation process (see Fig. 3c). Taking into account the experimentally determined phonon lifetimes (see Extended Data Fig. 1) and measured THz fields trajectories, leads to a remarkable agreement with the experimentally measured phonon angular momentum dynamics  $\mathbf{L}^{\text{R}}(t) = \mathbf{Q}^{\text{R}}(t) \times \dot{\mathbf{Q}}^{\text{R}}(t)$ . We find that  $\sim 3\%$  of the absolute  $E_u$  angular momentum is up-converted to the  $E_g$  mode at the  $\Gamma$ -point, while the remainder is likely dissipated into lower-energetic and higher-momentum acoustic modes, as sketched in the Fig. 3c inset. The coherent upconversion process, inverting the equilibration flow of angular momentum, provides the first direct observation of anharmonic phonon-phonon angular momentum transfer. In the following we will discuss the underlying angular momentum conservation rules in the classical field and quantum particle picture.

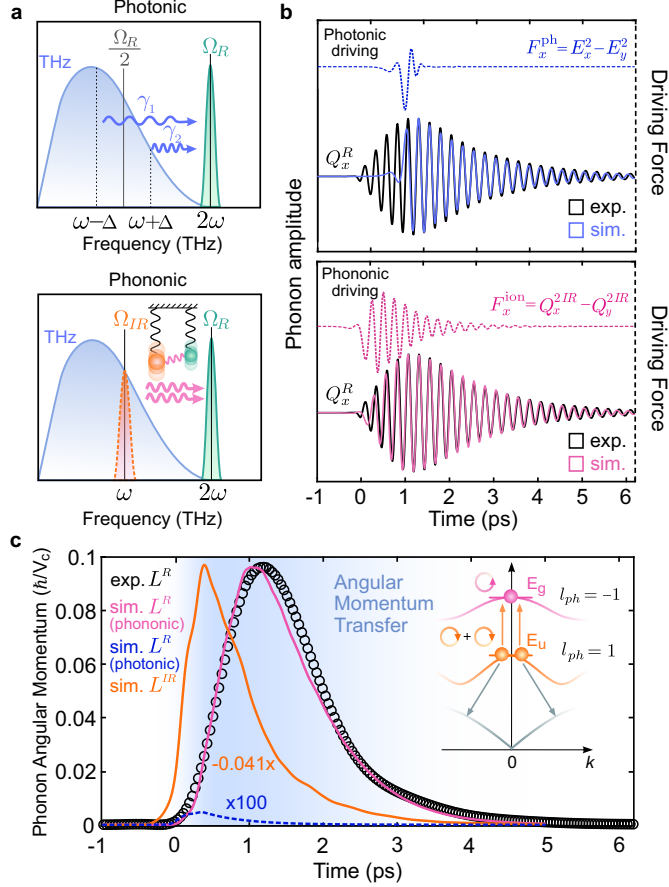


**Fig. 3 Angular momentum transfer channels and their dynamics.** **a**, Schematic of nonlinear excitation pathways. “Photonic” THz sum-frequency excitation (upper sketch): two spectral components of the THz pulse resonantly drive a Raman-active phonon at their sum frequency. “Phononic” sum-frequency ionic Raman scattering (lower sketch): A resonantly-driven IR-active phonon at half the Raman phonon frequency nonlinearly couples to a Raman-active phonon. **b**, Modelled dynamics of the photonic (blue, upper panel) and phononic (pink, lower panel) driving forces  $F_x$  (dotted lines, offset in time to match the phonon decay dynamics). A comparison of the resulting modelled phonon amplitudes  $Q_x^R$  (blue, pink) with the experimental data (black) under right-handed circular THz excitation reveals the dominant phononic excitation pathway of the  $E_g$  mode. **c**, Quantitative ab-initio modeling of angular momentum dynamics for all involved modes and pathways. The experimentally measured angular momentum dynamics  $L^R(t)$  (black circles) are normalized to the calculated phononic pathway  $L^R$  (pink) peak magnitude. The shaded blue area highlights angular momentum transfer from the  $E_u$  (orange) to the  $E_g$  (pink) mode, resulting in a delayed rise time and three orders of magnitude higher angular momentum transfer (pink) compared to photonic pathway (blue). Inset: About 3% of the  $E_u$  mode’s absolute angular momentum is transferred to the  $E_g$  mode, the rest likely dissipates into lower-energetic and higher-momentum modes.

## Discussion

In the classical picture, the symmetry allowed square-linear  $(Q^{\text{IR}})^2 Q^{\text{R}}$  coupling components lead to opposite helicities of the  $E_u$  mode and its nonlinear driving force,

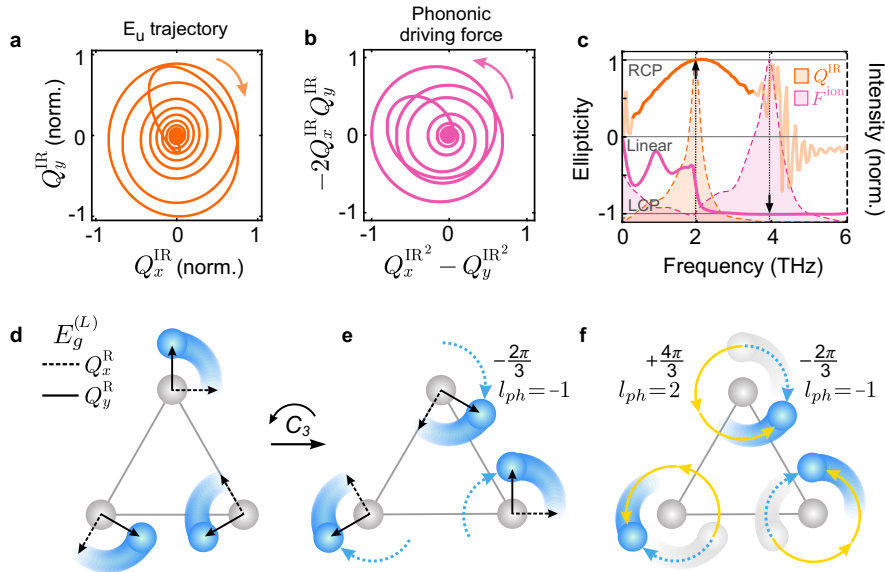


**Fig. 4 Conservation of phonon angular momentum.** **a-c**, Classical field picture: Helicity reversal dictated by the symmetry of anharmonic lattice potential. **a**,  $E_u$  phonon trajectory (orange) calculated based on the experimental RCP THz excitation field. **b**, Corresponding phononic driving force (pink) for the  $E_g$  mode, rotating in the opposite direction. **c**, Frequency-decomposed ellipticity of the  $E_u$  phonon  $Q^{\text{IR}}$  (pink) and its phononic driving force  $F^{\text{ion}}$  (orange) showing opposite helicities at 2 and 4 THz, respectively. **d-f**, PAM conservation in the particle picture under three-fold rotational invariance. **d**, Definition of quantized PAM in a triangular symmetry. Solid and dashed black arrows indicate the orthogonal components of a doubly-degenerate E-mode. All lattice sites are in phase in case of a  $\Gamma$ -mode. **e**, Under three-fold rotation, the crystal remains invariant up to a phase factor of  $l_{\text{ph}}2\pi/3$ , which defines the PAM to  $l_{\text{ph}} = -1$  here. **f**, Equivalence of  $l_{\text{ph}} = -1$  and  $l_{\text{ph}} = +2$  in three-fold symmetric groups.  $l_{\text{ph}} = +2$  is provided by the two-phonon absorption, corresponding to a rotational three-phonon Umklapp scattering.

as modelled in Figs. 4a,b, respectively. This becomes more obvious when moving to a circular basis  $Q_{|R\rangle/|L\rangle} = (Q_x \pm iQ_y)/\sqrt{2}$ , which turns the driving force into  $F_{|R\rangle/|L\rangle} = (F_x \pm iF_y)/\sqrt{2}$  and thus

$$F_{|R\rangle/|L\rangle} = c(Q_{|L\rangle/|R\rangle}^{\text{IR}})^2. \quad (2)$$

From this it is clear that the nonlinear phonon-phonon coupling doubles the frequency and inverts the helicity to enforce energy and angular momentum conservation, respectively (see Fig. 4c).

Turning to the quasi-particle picture, we evoke the definition of spin PAM  $l_{\text{ph}}$  as a conserved quantity under the  $C_3$  rotational symmetry of  $\text{Bi}_2\text{Se}_3$  [39]:

$$\hat{C}_3\phi_l(\varphi) = e^{i\frac{2\pi}{3}l_{\text{ph}}}\phi_l(\varphi), \quad (3)$$

where  $\phi_l$  is the wave function of the phonon at the high symmetry point  $k = 0$ . It is instructional to depict the two orthogonal components of the  $E_g$  mode under  $C_3$

symmetry on the simplest triangle lattice [27], as shown in Fig. 4d. As the axial mode is a superposition of two linearly polarized  $\Gamma$ -point modes, the  $Q_x$  and  $Q_y$  components have identical phase relations at each of the three lattice sites. After applying an in-plane  $C_3$  rotation (see Fig. 4e), an additional  $\pi/3$  phase factor has to be applied to obtain the initial eigenstate of Fig. 4d. Simply speaking, the ions have to go a third of their oscillation period backwards in time to reach the same position as a  $C_3$  rotation of a time snapshot. By definition in Eq. (3), the PAM is thus  $l_{\text{ph}} = -1$  per phonon for the observed LCP  $E_g$  mode. From the same equation this  $C_3$  symmetry  $l_{\text{ph}} = -1$  is equivalent to  $l_{\text{ph}} = 2$ , corresponding to an Umklapp process in a rotational Brillouin zone [34, 39]. Or, simply speaking, in a triangular lattice as depicted in Fig. 4f, we may either move  $4\pi/3$  of the phonon phase forward or  $2\pi/3$  backwards in time to reconstruct the phonon wave function after the  $C_3$  operation. In nonlinear phononics, the  $E_g$  amplitude scales with the square of the  $E_u$  driving mode, and thus also inherits twice its phase:  $Q^{\text{R}} \propto (Q^{\text{IR}})^2 = e^{i2\phi_{\text{IR}}} (\hat{Q}^{\text{IR}})^2$ . In the analogue particle picture, energy and PAM conservation of two annihilated  $E_u$  phonon quanta with  $l_{\text{ph}}^{\text{IR}} = 1$ , dictate that the  $E_g$  phonon must carry twice the energy and PAM of the  $E_u$  phonon, and thus  $l_{\text{ph}}^{\text{R}} = 2l_{\text{ph}}^{\text{IR}} = -1$ . The experimental reversal of phonon helicity thus shows that PAM is not only transferred but also perfectly conserved through anharmonic phonon-phonon coupling.

Most generally, our experimental observation confirms the long-standing hypothesis: Phonon-phonon angular momentum transfer is permitted via lattice anharmonicity and perfectly fulfills PAM conservation. This has far reaching implications for spin-relaxation phenomena, such as ultrafast demagnetization, and eventually identifies one of the unknown intermediate steps of the Einstein - de Haas and Barnett effects [10, 11, 28]. Our findings suggest that "natural" incoherent angular momentum dissipation from higher energy to lower energy (and potentially higher linear momentum) modes follows a similar anharmonic coupling mechanism that we follow here for the upconversion counterpart. This motivates higher momentum probing techniques like ultrafast electron [40, 41] or X-ray [14] diffraction to study the incoherent relaxation of phonon-phonon angular momentum transfer.

The demonstrated coherent angular momentum and energy upconversion, moreover opens the field of helical or chiral nonlinear phononics for selective control chiral states of matter. Our observations in the topological insulator  $\text{Bi}_2\text{Se}_3$ , directly enables studies on PAM phonon-driven control of topological surface states via spin-selective electron-phonon scattering [42] and will stimulate novel possibilities for phonon-driven topology switching [43]. Furthermore, the witnessed rotational phonon-phonon Umklapp scattering may play a similarly fundamental role for angular momentum dissipation and thermal Hall conductivity [5], as does the linear momentum Umklapp processes in heat transport [44]. Our observation of back-folded PAM states motivate further studies on phonon rotational Bloch functions and phonon driven Floquet matter [45], with potential implications on topological phonon states [46], active control of spin-valley polarization [1], or phonon orbital angular momentum states [47].

In conclusion, in full analogy to energy and linear momentum, our results experimentally confirm: transfer and conservation of phonon angular momentum is mediated by the anharmonicity of the crystal lattice. In the classical field picture, the rotational

symmetry imprinted in the anharmonic lattice potential, enforces the observed helicity switch between the two coupled modes. In the quasi-particle picture, phonon PAM is transferred and conserved by a rotational Umklapp process during three phonon scattering. This concept can be extended to any higher order lattice anharmonicity and multi-phonon scattering, therefore completing the solid state physics picture of axial and chiral phonons as quasi-particles responsible for carrying lattice angular momentum.

## Methods

### Sample details

The sample was grown on a sapphire (0001) substrate by means of molecular-beam epitaxy. Prior to the growth of the  $\text{Bi}_2\text{Se}_3$  epilayer, the sapphire substrate was annealed at  $900^\circ\text{C}$  for 30 minutes. Subsequently, the substrate temperature was reduced to  $270^\circ\text{C}$  for the growth of the  $\text{Bi}_2\text{Se}_3$  film, which took place in a Se overpressure regime. The Bi and Se partial pressures amount to  $5.31 \times 10^{-8}$  mbar and  $5.81 \times 10^{-7}$ , respectively, which results in a growth rate of 18.3 nm/h.

The sample was ex-situ characterized by x-ray diffraction, employing a Rigaku SmartLab XRD system. The film thickness was determined by means of x-ray reflectivity, shown in Fig. S1. Numerous oscillations are seen in the XRR curve, evidencing the high surface and interface quality of the  $\text{Bi}_2\text{Se}_3$  film. From the periodicity of the oscillations, a  $\text{Bi}_2\text{Se}_3$  film thickness of 15.0 nm is determined. To obtain information about the epilayer's crystal structure, XRD measurements were performed (Fig. S2). Besides the three peaks stemming from the sapphire substrate, a total of seven (0,0,1) peaks from the  $\text{Bi}_2\text{Se}_3$  epilayer are seen, proving the single-crystal nature of the  $\text{Bi}_2\text{Se}_3$  film with the *c*-axis in growth direction.

### Experimental setup

The experimental setup is shown in Extended Data Fig. 2a. Intense single-cycle THz pulses (1.5 THz central frequency, 2.0 THz spectral FWHM, 1 kHz repetition rate) with peak fields exceeding 1.5 MV/cm are generated by optical rectification in  $\text{LiNbO}_3$  using the tilted pulse front technique [48]. Synchronized optical probe pulses (790 nm central wavelength, 1.6 nJ pulse energy, 80 MHz repetition rate, 20 fs pulse duration) are collinearly incident on the sample at normal incidence. The probe polarization angle is controlled using a half-wave plate to resolve the two orthogonal components of the  $E_g$  phonon mode (Fig. 1f). The intense THz pulses induce a transient birefringence in the sample, which alters the polarization of the transmitted optical probe pulses (THz-induced Kerr effect, TKE [49]) Coherently excited Raman-active phonons contribute to this transient birefringence by modulating the linear susceptibility [32, 33]. A balanced detection scheme comprising a half-wave plate, Wollaston prism, and balanced photodiodes is used to measure this change in polarization.

## Helicity-tailored THz fields

To control the THz polarization state, we use a birefringent 700 $\mu\text{m}$ -thick y-cut quartz waveplate that imparts a frequency-dependent relative phase retardation between the orthogonal fast and slow crystalline axes (Fig. S3 a,b). Due to the highly polychromatic nature of a single-cycle THz pulse, the waveplate generates a continuum of elliptical polarization states across the broad spectrum constituting the pulse, but is tailored to have a particular thickness to generate the desired circular polarization state at 2 THz, where the  $E_u$  phonon resonance is situated. By orienting the quartz waveplate to  $0^\circ$ ,  $-45^\circ$ ,  $+45^\circ$  with respect to the vertical incident THz polarization, the transmitted THz polarization state is toggled between linear, right, and left-circular polarizations at 2 THz. In addition, to investigate the intermediate state of arbitrary elliptical atomic trajectories (Extended Data Fig.5l), we use a 380 $\mu\text{m}$ -thick y-cut quartz waveplate (Fig.S3 c,d), enabling excitation with an elliptically polarized THz beam (Extended Data Fig.5 a,b).

## Measuring $E_u$ phonon lifetime via THz transmission

We employ THz time-domain spectroscopy in a double-focus geometry, shown in Extended Data Fig. 1a, to measure the THz transmission of a  $\text{Bi}_2\text{Se}_3$  film. A spintronic THz emitter (TeraSpinTech T-Spin2) generates an ultrabroadband THz pulse [50], which is focused onto the sample in the first focal position. The transmitted THz pulse is then refocused onto a 30  $\mu\text{m}$ -thick GaP crystal for electro-optic sampling. To determine the intrinsic THz transmission  $T_{\text{Bi}_2\text{Se}_3}(\omega)$  of  $\text{Bi}_2\text{Se}_3$ , we conduct two measurements: (1) the THz transmission of a 0.3  $\mu\text{m}$ -thick  $\text{Bi}_2\text{Se}_3$  film grown on a 500  $\mu\text{m}$  sapphire substrate and (2) a reference THz transmission through an identical 500  $\mu\text{m}$ -thick sapphire wafer (Extended Data Fig. 1b,c). Taking the ratio of these spectra eliminates the detector response function of the GaP crystal, and partially removes the substrate contribution, therefore containing the intrinsic THz transmission properties of  $\text{Bi}_2\text{Se}_3$  (Extended Data Fig. 1d). The resultant characteristic absorption feature at 2 THz confirms the dominant absorption due to the excitation of the IR-active  $E_u$  phonon mode.

We identify an analytical expression for the THz transmission function  $T_{\text{Bi}_2\text{Se}_3}(\omega)$  based on Fresnel coefficients, incorporating the  $\text{Bi}_2\text{Se}_3$  dielectric function to extract the  $E_u$  phonon frequency  $\omega_{\text{IR}}$  and damping rate  $\gamma_{\text{IR}}$ , which defines the phonon lifetime  $\tau_{\text{IR}} = 1/\gamma_{\text{IR}}$ . The  $\text{Bi}_2\text{Se}_3$  transmission function is given by  $T_{\text{Bi}_2\text{Se}_3}(\omega) = T_{\text{total}}(\omega)/T_{\text{sapph}}(\omega)$ .

The theoretical reference transmission  $T_{\text{sapph}}(\omega)$  is calculated using a single-layer model that accounts for all internal reflections within the sapphire wafer

$$T_{\text{sapph}}(\omega) = \frac{t_{03}t_{30}e^{i\varphi_3}}{1 - r_{30}^2e^{i2\varphi_3}}. \quad (\text{M1})$$

The sample transmission function  $T_{\text{total}}(\omega)$  is derived using a four-layer interference model of the  $\text{Bi}_2\text{Se}_3$  film and the sapphire substrate, where the topological insulator  $\text{Bi}_2\text{Se}_3$  is represented by a three-layer model of an insulating bulk layer with

two conductive topological surface states (TSS) at the interfaces (see SI for extended discussion):

$$T_{\text{total}}(\omega) = \frac{T_{03}t_{30}e^{i\varphi_3}}{1 - r_{30}R_{30}e^{i2\varphi_3}}. \quad (\text{M2})$$

Here,  $t_{ij}(\omega)$  and  $r_{ij}(\omega)$  denote the Fresnel transmission and reflection coefficients for a wave propagating from medium  $i$  to medium  $j$ .  $T_{03}(\omega)$  and  $R_{30}(\omega)$  represent the joint transmission and reflection coefficients of the  $\text{Bi}_2\text{Se}_3$  sample, treated as a whole, including both the bulk and the TSS layers (Fig.S4). Indices 0 and 3 refer to air and sapphire, respectively, and  $\varphi_3(\omega)$  represents the phase accumulated by the THz pulse while propagating through the sapphire substrate.

The bulk dielectric function  $\varepsilon_{\text{bulk}}(\omega)$  is described using the Lorentz oscillator model, incorporating the contribution of the IR-active  $E_u$  phonon mode. The dielectric function of the surface layers  $\varepsilon_{\text{TSS}}(\omega)$  is defined by the Drude model to account for surface conductivity:

$$\varepsilon_{\text{bulk}}(\omega) = \varepsilon_{\infty} + \frac{S\omega_{\text{IR}}^2}{\omega_{\text{IR}}^2 - \omega^2 - i\gamma_{\text{IR}}\omega}, \quad (\text{M3})$$

$$\varepsilon_{\text{TSS}}(\omega) = 1 - \frac{\omega_{\text{pl}}^2}{\omega^2 + i\gamma\omega}. \quad (\text{M4})$$

The final transmission function  $T_{\text{Bi}_2\text{Se}_3}(\omega)$  accounts for multiple internal reflections within  $\text{Bi}_2\text{Se}_3$ , closely matching the measured transmission spectrum (Extended Data Fig. 1d). By modeling the experimental data, we identify the  $E_u$  phonon parameters to be  $\omega_{\text{IR}}=1.97$  THz and  $\gamma_{\text{IR}}=0.2$  THz, corresponding to the phonon lifetime  $\tau_{\text{IR}}=5$  ps.

## Helicity state characterization

We characterized the complex helicity states of the single-cycle THz pulses and arbitrarily polarized phonon states by computing the ellipticity parameter in the frequency domain. The ellipticity, which quantifies the relative contribution of circular polarization components, is calculated as the normalized third Stokes parameter  $S_3(\omega)$ , independently evaluated at each frequency. To achieve this, the electric field components  $E_x(\omega)$  and  $E_y(\omega)$  in the Cartesian basis  $(\hat{x}, \hat{y})$  are transformed into the circular basis  $(\hat{R}, \hat{L})$ . The corresponding field components in the circular basis are computed as  $E_R(\omega) = (E_x(\omega) + iE_y(\omega))/\sqrt{2}$  and  $E_L(\omega) = (E_x(\omega) - iE_y(\omega))/\sqrt{2}$ . The ellipticity parameter  $S_3(\omega)$  is then determined as  $S_3(\omega) = (|E_R|^2 - |E_L|^2)/E^2$ , where  $E^2 = |E_R|^2 + |E_L|^2$ . The parameter takes values in the range  $[-1, 1]$ , with  $S_3(\omega)=1$  corresponding to purely right-handed circular polarization (RCP),  $S_3(\omega)=-1$  to purely left-handed circular polarization (LCP), and  $S_3(\omega)=0$  to any possible linear polarization. The same procedure is applied to characterize the polarization state of a phonon with the amplitude  $Q(\omega) = (Q_x(\omega), Q_y(\omega))$ . This approach provides a frequency-resolved description of the helicity states for both THz pulses and phonon modes.

## Probing $E_g$ phonon trajectories

The coherent phonon dynamics of the  $E_g$  mode are monitored via the THz-induced Kerr effect, where the intense THz pulses induced transient optical birefringence in  $\text{Bi}_2\text{Se}_3$  sample, mediated by the coherent lattice vibration. As the optical probe pulse propagates through the sample, its polarization undergoes a time-dependent rotation proportional to the amplitude of the coherent phonon. We note that the temporal evolution of the  $E_g$  mode is thus measured by varying the time delay between the THz pump and optical probe pulses.

We note that the THz-induced Kerr effect involves a Raman-type probing mechanism [33], in which the THz pump and optical probe fields couple via the third-order nonlinear susceptibility to measure coherent phonon dynamics, analogous to stimulated Raman scattering experiments. In this regard, the Raman tensor formalism provides a framework for understanding the probing of phonon trajectories.

The probing signal  $S^{\text{pr}}$  of a phonon amplitude is dependent on the in-plane azimuthal angle and is determined by the phonon symmetry encoded in the Raman tensor. This Raman-type probing via transient birefringence can be expressed as  $S^{\text{pr}} \propto \hat{e}_i^{\perp\text{pr}} Q(t) R_{ij}^Q \hat{e}_j^{\text{pr}}(\theta)$ , where  $\hat{e}^{\text{pr}}$  and  $\hat{e}^{\perp\text{pr}}$  are the polarization vector of the incident probe pulse oriented at the angle  $\theta$  in the laboratory frame and a unit vector perpendicular to it, respectively.  $R_{ij}^Q$  is the Raman tensor of a given coherent phonon amplitude  $Q(t)$ .

In the case of a doubly degenerate mode, such as the  $E_g$  mode, two distinct Raman tensors are involved in the probing mechanism, corresponding to the two orthogonal components that form a basis for a polarization-resolved detection. In this representation, the probing signal is given by  $S^{\text{pr}} \propto \hat{e}_i^{\perp\text{pr}} (Q_1(t) R_{ij}^{Q_1} + Q_2(t) R_{ij}^{Q_2}) \hat{e}_j^{\text{pr}}(\theta)$ , where  $Q_1(t)$  and  $Q_2(t)$  are the classical amplitudes of the orthogonal phonon components,  $R_{ij}^{Q_1}$  and  $R_{ij}^{Q_2}$  are the corresponding Raman tensors in the laboratory frame  $(\hat{x}, \hat{y})$ . For the  $E_g$  phonon mode, the Raman tensors of two orthogonal projections  $Q_x(t)$  and  $Q_y(t)$  are given by [36, 51]

$$\mathbf{R}_x = \begin{pmatrix} c & 0 \\ 0 & -c \end{pmatrix}, \quad \mathbf{R}_y = \begin{pmatrix} 0 & -c \\ -c & 0 \end{pmatrix}. \quad (\text{M5})$$

Therefore, for a probe pulse with an incident polarization  $\hat{e}^{\text{pr}} = (-\sin\theta, \cos\theta)$ , which is aligned vertically at  $\theta=0^\circ$ , the resulting probing signal is given by  $S^{\text{pr}}(t, \theta) \propto Q_x(t) \sin 2\theta + Q_y(t) \cos 2\theta$ . This angular dependence reflects the quadrupolar symmetry of the  $E_g$  phonon mode and enables selective detection of its orthogonal components. By aligning the probe polarization to  $\theta=45^\circ$  and  $\theta=0^\circ$ , the contribution of  $Q_x(t)$  and  $Q_y(t)$  can be isolated (Extended Data Fig. 3c), respectively, allowing for the reconstruction of the  $E_g$  phonon trajectory, similar as in [27]. Note that all TKE and polarization-resolved EOS measurements use the same probe polarizations to resolve the x- and y-components of the  $E_g$  phonon state and THz pump field, respectively. This results from the shared three-fold rotational symmetry property of  $\text{Bi}_2\text{Se}_3$  ( $D_{3d}$  point group) and the  $\alpha$ -quartz EOS detector crystal ( $D_3$  point group), allowing a direct and straightforward comparison between the THz and phonon polarization states in the same laboratory frame, enabling unambiguous identification of helicity reversal.

## Excitation pathways of the $E_g$ mode

The higher-frequency Raman-active  $E_g$  phonon mode can be driven via two distinct pathways: photonic sum-frequency excitation [35] and ionic Raman scattering [30] through anharmonic coupling with IR-active  $E_u$  phonon. The temporal evolution of the doubly-degenerate  $E_g$  phonon amplitude can be described classically by a system of two equations of motion with the vectorial driving force  $\vec{F}(t)$

$$\ddot{Q}_i^R + \gamma_R \dot{Q}_i^R + \omega_R^2 Q_i^R = F_i(t), \quad i = \{x, y\}, \quad (\text{M6})$$

where  $Q^R$  is the coherent amplitude of the  $E_g$  mode.

In the photonic pathway, the THz field  $\vec{E}^{\text{THz}} = (E_x, E_y)$  directly couples to the Raman tensors of the  $E_g$  mode, yielding a driving force:

$$\vec{F}_R^{\text{ph}} \propto \begin{pmatrix} R_x^{ij} E_i E_j \\ R_y^{ij} E_i E_j \end{pmatrix} = c \begin{pmatrix} E_x^2 - E_y^2 \\ -2E_x E_y \end{pmatrix}. \quad (\text{M7})$$

In the phononic pathway, the driving force originates from the anharmonic potential of the Raman-active  $E_g$  mode and the IR-active  $E_u$  mode at half its frequency. This mechanism is known as sum-frequency ionic Raman scattering. The lowest-order symmetry-allowed anharmonic potential coupling the Raman-active  $E_g$  and the IR-active  $E_u$  modes is given by:

$$V_{\text{anh}}(Q^{\text{IR}}, Q^{\text{R}}) = d[(Q_x^{\text{IR}})^2 - (Q_y^{\text{IR}})^2]Q_x^{\text{R}} - 2dQ_x^{\text{IR}}Q_y^{\text{IR}}Q_y^{\text{R}} + O(Q^4), \quad (\text{M8})$$

where  $Q^{\text{IR}}$  and  $Q^{\text{R}}$  are coherent phonon amplitudes of  $E_u$  and  $E_g$  axial phonon states, respectively. This simplest form of the potential results in phononic driving force acting of the  $E_g$  mode:

$$\vec{F}_R^{\text{ion}} \propto \begin{pmatrix} -\partial V_{\text{anh}}/\partial Q_x^{\text{R}} \\ -\partial V_{\text{anh}}/\partial Q_y^{\text{R}} \end{pmatrix} = -d \begin{pmatrix} (Q_x^{\text{IR}})^2 - (Q_y^{\text{IR}})^2 \\ -2Q_x^{\text{IR}}Q_y^{\text{IR}} \end{pmatrix}. \quad (\text{M9})$$

The photonic (M7) and phononic (M9) driving forces exhibit identical spatial-rotational symmetry, as the THz field and the IR-active  $E_u$  mode both necessarily transform as a vector representation within the  $D_{3d}$  point group of the  $\text{Bi}_2\text{Se}_3$  crystal lattice. While the forces' spatial symmetries are the same, their temporal profiles differ: the photonic driving force follows the duration of the single-cycle THz pulse, whereas the phononic driving force is governed, for short THz excitation pulses, by the lifetime of the IR-active  $E_u$  phonon, setting the timescale for phonon-phonon coupling (Extended Data Fig. 4b).

The differing durations of the driving forces result in distinctly different rise times in the  $E_g$  phonon evolution. To identify the dominant excitation mechanism, we analyze the rise time of the measured  $E_g$  phonon dynamics and model both excitation pathways. For the photonic driving case, we calculate the  $E_g$  phonon evolution  $Q^{\text{R}}(t)$  by solving the equation of motion (M6) with the driving force defined in (M7), using the electric field components of the circularly polarized THz field measured by

polarization-resolved EOS (Fig. 1e). The damping rate  $\gamma_R$  used here is identified from the TKE signal ( $\gamma_R=0.22$  THz).

To model the phononic case, we first solve the system of four equations corresponding to the polarization components of the  $E_u$  and  $E_g$  phonon modes  $Q = \{Q_x^{\text{IR}}, Q_y^{\text{IR}}, Q_x^{\text{R}}, Q_y^{\text{R}}\}$ . Here, the IR-active mode is linearly driven by the same circularly-polarized THz pulse (Fig. 1e) and coupled with the Raman-active mode via anharmonic potential  $V_{\text{anh}}(\mathbf{Q}^{\text{IR}}, \mathbf{Q}^{\text{R}})$ , so its driving force's components are defined as  $F_i^{\text{IR}} = E_i^{\text{THz}} - \partial V_{\text{anh}} / \partial Q_i^{\text{IR}}$ . The driving force acting on the  $E_g$  mode is purely defined by the anharmonic coupling potential  $F_i^{\text{R}} = -\partial V_{\text{anh}} / \partial Q_i^{\text{R}}$ . The parameters for the  $E_u$  phonon mode ( $\omega_{\text{IR}}=1.97$  THz,  $\gamma_{\text{IR}}=0.20$  THz) are obtained from THz transmission measurements (see "THz transmission analysis of  $E_u$  phonon lifetime") and the  $E_g$  phonon damping rate is identified from the TKE signal decay dynamics ( $\gamma_R=0.29$  THz).

By comparing the modeled dynamics with the experimental data, we identify the phononic pathway as the dominant mechanism (Fig. 3b).

## Theory of phonon angular momentum upconversion

The equations of motion describing the coherent driving of phonon modes can be expressed as [30]

$$\ddot{Q}_\alpha + \gamma_\alpha \dot{Q}_\alpha + \partial_{Q_\alpha} V = \sum_i Z_{i,\alpha} E_i + \epsilon_0 \sum_{ij} R_{ij,\alpha} E_i E_j, \quad (\text{M10})$$

where  $Q_\alpha$  is the phonon amplitude,  $\gamma_\alpha$  is the phonon linewidth, and  $V$  is the phonon potential energy. The index  $\alpha = \{E_u^a, E_u^b, E_g^a, E_g^b\}$  denotes the two orthogonal branches of each of the doubly degenerate  $E_u$  and  $E_g$  modes. We note here that this ab-initio theoretical treatment, which is referenced to the crystalline axes (a,b), is connected to the experimental (i.e., labframe coordinates - x,y) description by the relative rotational invariance of the forces, which follows from the rotational symmetry of the system. The right-hand side of the equation contains the light-matter interactions. The first term describes infrared absorption and contains the mode effective charge,  $\mathbf{Z}_\alpha$ , given by

$$\mathbf{Z}_\alpha = \sum_n Z_n^* \frac{\mathbf{q}_{n,\alpha}}{\sqrt{M_n}}, \quad (\text{M11})$$

where  $Z_n^*$  is the Born effective charge tensor of atom  $n$ ,  $\mathbf{q}_{n,\alpha}$  is its phonon eigenvector, and  $M_n$  its atomic mass, and the sum runs over all atoms in the unit cell. The second term describes Raman scattering and contains the Raman tensors,  $R_{ij}$ , given by

$$R_{ij,\alpha} = V_c \frac{\partial \epsilon_{ij}}{\partial Q_\alpha}, \quad (\text{M12})$$

where  $\epsilon_{ij}$  is the dielectric function,  $V_c$  the volume of the unit cell and  $i, j$  denote the spatial coordinates.  $\mathbf{E}(t)$  represents the electric field component of the laser pulse, polarized in the  $ab$  plane of the crystal according to the experimental setup. Using the

Bilbao Crystallographic Server, we find that the Raman tensors of the  $E_g$  modes,  $E_g^a$  and  $E_g^b$ , take the following form

$$R_{E_g^a} = \begin{pmatrix} R & 0 \\ 0 & -R \end{pmatrix}, \quad (\text{M13})$$

$$R_{E_g^b} = \begin{pmatrix} 0 & -R \\ -R & 0 \end{pmatrix}. \quad (\text{M14})$$

Because of the symmetry group of the crystal it is possible to choose the coordinates  $Q_{E_g^a}$  and  $Q_{E_g^b}$  such that they transform, respectively, as  $Q_{E_u^a}^2 - Q_{E_u^b}^2$  and  $Q_{E_u^a} Q_{E_u^b}$ . With this choice the phonon potential energy including anharmonic contributions reads:

$$V = \frac{\Omega_{E_u}^2}{2}(Q_{E_u^a}^2 + Q_{E_u^b}^2) + \frac{\Omega_{E_g}^2}{2}(Q_{E_g^a}^2 + Q_{E_g^b}^2) + cQ_{E_g^a}(Q_{E_u^a}^2 - Q_{E_u^b}^2) + 2cQ_{E_g^b}Q_{E_u^a}Q_{E_u^b} + \tilde{V}. \quad (\text{M15})$$

Here,  $\Omega_{E_u}$  and  $\Omega_{E_g}$  are the eigenfrequencies of the IR-active  $E_u$  and Raman-active  $E_g$  modes, respectively, while the three-phonon coupling  $c$  denotes the nonlinear phonon coupling of primary interest here.  $\tilde{V}$  contains higher order anharmonicities and nonlinear phonon couplings up to fourth order, as dictated by the  $\bar{3}m$  point-group symmetry,

$$\begin{aligned} \tilde{V} = & d_a Q_{E_u^a}^4 + d_b Q_{E_u^b}^4 + d_c Q_{E_g^a}^4 + d_d Q_{E_g^b}^4 \\ & + d_{ab} Q_{E_u^a}^2 Q_{E_u^b}^2 + d_{ac} Q_{E_g^a}^2 Q_{E_u^b}^2 + d_{ad} Q_{E_g^b}^2 Q_{E_u^b}^2 + d_{bc} Q_{E_g^b}^2 Q_{E_u^a}^2 + d_{bd} Q_{E_g^a}^2 Q_{E_u^b}^2 \\ & + d_{abc} Q_{E_g^a}^2 Q_{E_u^a} Q_{E_u^b} + d_{abd} Q_{E_g^b}^2 Q_{E_u^a} Q_{E_u^b}. \end{aligned} \quad (\text{M16})$$

Ionic Raman scattering (IRS) is described by three-phonon coupling between two IR-active phonons and one Raman-active phonon, as in Eq. (M15). The combined dynamics of the  $E_u$  and  $E_g$  modes for this process can be obtained by solving the coupled equations of motion resulting from Eq. (M10) with  $R_{ij} = 0$  and the phonon potential  $V$  given by Eq. (M15). The equations of motion then read

$$\ddot{Q}_{E_u^a} + \kappa_{E_u} \dot{Q}_{E_u^a} + \Omega_{E_u}^2 Q_{E_u^a} = Z_{E_u^a, x} E_x(t) + 2cQ_{E_u^a} Q_{E_g^a} - 2cQ_{E_u^b} Q_{E_g^b} - \partial_{Q_{E_u^a}} \tilde{V}, \quad (\text{M17})$$

$$\ddot{Q}_{E_u^b} + \kappa_{E_u} \dot{Q}_{E_u^b} + \Omega_{E_u}^2 Q_{E_u^b} = Z_{E_u^b, y} E_y(t) - 2cQ_{E_u^b} Q_{E_g^a} - 2cQ_{E_u^a} Q_{E_g^b} - \partial_{Q_{E_u^b}} \tilde{V}, \quad (\text{M18})$$

$$\ddot{Q}_{E_g^a} + \kappa_{E_g} \dot{Q}_{E_g^a} + \Omega_{E_g}^2 Q_{E_g^a} = -c(Q_{E_u^b}^2 - Q_{E_u^a}^2) - \partial_{Q_{E_g^a}} \tilde{V}, \quad (\text{M19})$$

$$\ddot{Q}_{E_g^b} + \kappa_{E_g} \dot{Q}_{E_g^b} + \Omega_{E_g}^2 Q_{E_g^b} = -2cQ_{E_u^a} Q_{E_u^b} - \partial_{Q_{E_g^b}} \tilde{V}. \quad (\text{M20})$$

In contrast, for terahertz sum-frequency excitation (THz-SFE), we consider a purely harmonic phonon potential, as anharmonicities are not significant in this process. Thus, only the harmonic terms from Eq. (M15) contribute to the equations of

motion. Furthermore, in centrosymmetric crystals  $\mathbf{Z}_\alpha = 0$  for Raman-active phonons, and Eq. (M10) accordingly simplifies to:

$$\ddot{Q}_{E_g^a} + \kappa_{E_g} \dot{Q}_{E_g^a} + \Omega_{E_g}^2 Q_{E_g^a} = \epsilon_0 R (E_x^2(t) - E_y^2(t)), \quad (\text{M21})$$

$$\ddot{Q}_{E_g^b} + \kappa_{E_g} \dot{Q}_{E_g^b} + \Omega_{E_g}^2 Q_{E_g^b} = -2\epsilon_0 R E_x(t) E_y(t). \quad (\text{M22})$$

The two processes differ in the driving force that the coherently excited  $E_u$  modes produce for the the Raman-active  $E_g$  modes. In THz-SFE, the driving force is the square of the electric field (see Eqs. (M21) and (M22)). In contrast, for IRS, the primary component of the driving force is proportional to the square of the IR-active phonon amplitude (see Eqs. (M19) and (M20)).

Finally, the mechanical angular momentum produced by the phonon modes can be obtained in terms of the phonon amplitudes [23]

$$\mathbf{L} = \mathbf{Q}_\alpha \times \dot{\mathbf{Q}}_\alpha, \quad (\text{M23})$$

where the amplitude vectors are given by  $\mathbf{Q}_{E_u} = (Q_{E_u^a}, Q_{E_u^b}, 0)$  and  $\mathbf{Q}_{E_g} = (Q_{E_g^a}, Q_{E_g^b}, 0)$ , respectively.

## First-principles calculations

We calculated the phonon eigenfrequencies, eigenvectors, Born effective charges and dielectric function of  $\text{Bi}_2\text{Se}_3$  using the density functional theory formalism as implemented in VASP, as well as the frozen-phonon method as implemented in PHONOPY. We used PAW pseudopotentials with valence electron configurations  $\text{Bi}(6s^26p^3)$  and  $\text{Se}(4s^24p^4)$ , and we used the PBEsol form of the generalized gradient approximation (GGA) for the exchange-correlation functional. No Hubbard or Hund's exchange correction was added. We converged the Hellmann-Feynman forces to  $10^{-5}$  eV/Å using a plane-wave energy cutoff of 500 eV and a  $11 \times 11 \times 11$  k-point mesh. The lattice constants of our fully relaxed structure,  $a = 4.13$  Å and  $c = 28.6$  Å, fit reasonably well to experimental values.

To determine the single-mode anharmonicities and nonlinear phonon couplings, we computed the total energy of the system on a  $11 \times 11 \times 11$  grid of atomic displacements along the eigenvectors of each of the phonon modes,  $Q_{E_u^a}$ ,  $Q_{E_u^b}$ ,  $Q_{E_g^a}$  and  $Q_{E_g^b}$ , and fitted the resulting potential energy landscape to the phonon potential energy,  $V$ . To control the displacement direction, we rotated the mode-effective charge vectors of the  $E_u$  modes to align them with the  $x$  and  $y$  axes. This rotation mixes the eigenvectors, weighted by the rotation matrix elements, which were then used to generate the displacement grid. For the  $E_g$  modes, we applied a rotation such that the resulting Raman tensors correspond to Eq. (M13) and Eq. (M14). To compute the Raman tensors, we determined the static dielectric function from DFT calculations using VASP and evaluated the tensors as derivatives of the dielectric function with respect to the Raman phonon amplitudes (see Eq. (M12)). We obtained a value of  $R = 232 \text{ Å}^2/\sqrt{u}$ , was obtained, where  $u$  is the atomic mass unit.

**Table 1** Calculated eigenfrequencies in THz, single-mode anharmonicities and nonlinear phonon couplings in  $\text{meV}/(\text{\AA}\sqrt{u})^n$ ,  $n$  being the order of the phonon amplitude and  $u$  the atomic mass unit, and mode effective charges in  $e/\sqrt{u}$ , where  $e$  is the elementary charge.

	$c_{abc}$	$c_{abd}$	$c_{ac}$	$c_{ad}$	$c_{bc}$	$c_{bd}$	$d_a$	$d_b$	$d_c$	$d_d$	$d_{ab}$	$d_{ac}$	$d_{ad}$	$d_{bc}$	$d_{bd}$	$d_{abc}$	$d_{abd}$	$Z$
$E_u^a(2.6)$							0.3				0.5							1.04
$E_u^b(2.6)$								0.3			0.5							1.04
$E_g^a(4.2)$	-1.1		1.3		-1.3				-0.02			-0.02		0.2		-1.1		0
$E_g^b(4.2)$		-2.6		-0.6		0.6				-0.02			0.2	-0.02			0.2	0

The general anharmonic phonon potential energy we used for fitting reads

$$\begin{aligned}
V = & \frac{\Omega_{E_u}^2}{2}(Q_{E_u^a}^2 + Q_{E_u^b}^2) + \frac{\Omega_{E_g}^2}{2}(Q_{E_g^a}^2 + Q_{E_g^b}^2) \\
& + d_a Q_{E_u^a}^4 + d_b Q_{E_u^b}^4 + d_c Q_{E_g^a}^4 + d_d Q_{E_g^b}^4 \\
& + c_{abc} Q_{E_g^a} Q_{E_u^a} Q_{E_u^b} + c_{abd} Q_{E_g^b} Q_{E_u^a} Q_{E_u^b} \\
& + c_{ac} Q_{E_g^a} Q_{E_u^a}^2 + c_{ad} Q_{E_g^b} Q_{E_u^a}^2 + c_{bc} Q_{E_g^a} Q_{E_u^b}^2 + c_{bd} Q_{E_g^b} Q_{E_u^b}^2 \\
& + d_{ab} Q_{E_u^a}^2 Q_{E_u^b}^2 + d_{ac} Q_{E_g^a}^2 Q_{E_u^a}^2 + d_{ad} Q_{E_g^b}^2 Q_{E_u^a}^2 + d_{bc} Q_{E_g^b}^2 Q_{E_u^b}^2 + d_{bd} Q_{E_g^a}^2 Q_{E_u^b}^2 \\
& + d_{abc} Q_{E_g^a}^2 Q_{E_u^a} Q_{E_u^b} + d_{abd} Q_{E_g^b}^2 Q_{E_u^a} Q_{E_u^b}. \tag{M24}
\end{aligned}$$

This general potential with mixed components of the doubly degenerate modes can be brought back into the form of Eq. (M15) with a coordinate transformation. Next, we computed the total energy on a  $11 \times 11 \times 11$  grid defined by atomic displacements along the eigenvectors of the rotated  $E_u$  and  $E_g$  modes. The resulting anharmonic potential explicitly includes coupling terms between the doubly degenerate  $E_u$  modes and each of the  $E_g$  modes separately, while no coupling is considered between the individual  $E_g$  modes themselves, which is deemed to be small.

We performed a three-step fitting procedure on the resulting potential energy landscape to extract single-mode anharmonicities and nonlinear phonon couplings from the phonon potential energy  $V$  in Eq. (M24). First, we obtained the single-mode anharmonicities for the  $E_u$  and  $E_g$  modes by fitting the potential energy landscape for each mode individually. We used the total energy from the grid points where displacements occurred along a single-phonon mode, with the others fixed to zero. From this, we obtained the coefficients  $\Omega_{E_u}, \Omega_{E_g}, d_a, d_b, d_c, d_d$ . We include the phonon frequencies in the fitting to ensure that they match those computed with PHONOPY. Next, we focused on the term that involved only the  $E_u$  modes,  $Q_{E_u^a}^2 Q_{E_u^b}^2$ , by fitting the potential energy landscape to the total energy values where only the  $E_u$  modes were displaced, with the  $E_g$  modes held at zero. The single-mode anharmonicities of the first step were kept fixed, allowing us to extract the coefficient  $d_{ab}$ . Finally, we fitted the potential energy landscape to the terms in  $V$  (in Eq. (M24)) that involve the three phonon modes for each of the  $E_g$  modes, using total energy values from the grid points where all modes were displaced. With the coefficients from the previous steps held constant, we determined the nonlinear phonon couplings  $d_{ac}, d_{ad}, d_{bc}, d_{bd}, d_{abc}, d_{abd}$ . Table 1 summarizes the computed phonon properties and anharmonic coefficients.

## Angular Momentum Conservation

The observed helicity reversal of the  $E_g$  modes arises from angular momentum conservation between the  $E_u$  and  $E_g$  modes in the three-fold crystal lattice, which dictates the form of the driving force. Specifically, the phononic driving force originates from the symmetry-allowed coupling between the IR-active  $E_u$  mode (transforming as a vector under the  $D_{3d}$  point group) and the Raman-active  $E_g$  mode (transforming as a symmetric second-rank tensor). Consequently, the driving force acquires the opposite helicity of the  $E_u$  phonon generating it. This helicity reversal is shown in Fig. 4a-c, where Fig.4a depicts the trajectory of the  $E_u$  phonon, and Fig.4b illustrates the resulting force acting on the  $E_g$  mode, rotating in the opposite direction and thus carrying an inverted angular momentum (Fig.4c). A detailed step-by-step modeling of the  $E_g$  phonon dynamics, demonstrating the helicity flip, is provided in Extended Data Fig. 5.

The change of the helicity state becomes more evident when transforming from the Cartesian basis  $(\hat{x}, \hat{y})$  to a circular basis  $(\hat{R}, \hat{L})$ . In the Cartesian basis, the driving force components are given by:

$$F_x^{\text{ion}} = c [Q_x^{\text{IR}^2} - Q_y^{\text{IR}^2}], \quad F_y^{\text{ion}} = -2c Q_x^{\text{IR}} Q_y^{\text{IR}}. \quad (\text{M25})$$

To express the force in terms of circularly polarized states, we rewrite the phonon components and the corresponding driving as:

$$Q_{|R\rangle}^{\text{IR}} = \frac{1}{\sqrt{2}} [Q_x^{\text{IR}} + iQ_y^{\text{IR}}], \quad Q_{|L\rangle}^{\text{IR}} = \frac{1}{\sqrt{2}} [Q_x^{\text{IR}} - iQ_y^{\text{IR}}], \quad (\text{M26})$$

$$F_{|R\rangle}^{\text{ion}} = \frac{1}{\sqrt{2}} [F_x^{\text{ion}} + iF_y^{\text{ion}}], \quad F_{|L\rangle}^{\text{ion}} = \frac{1}{\sqrt{2}} [F_x^{\text{ion}} - iF_y^{\text{ion}}]. \quad (\text{M27})$$

Here,  $Q_{|R\rangle}^{\text{IR}}$  and  $Q_{|L\rangle}^{\text{IR}}$  are the right- and left-handed circularly polarized states of the  $E_u$  phonon, while  $F_{|R\rangle}^{\text{ion}}$  and  $F_{|L\rangle}^{\text{ion}}$  represent the phononic forces driving the corresponding right- and left-handed circular polarized states of the  $E_g$  mode, respectively. In the circular basis, the driving force takes the form:

$$F_{|R\rangle}^{\text{ion}} = c Q_{|L\rangle}^{\text{IR}^2}, \quad F_{|L\rangle}^{\text{ion}} = c Q_{|R\rangle}^{\text{IR}^2}. \quad (\text{M28})$$

In the circular basis, it becomes clear that the left-circularly polarized component of the  $E_u$  phonon drives the right-circularly polarized  $E_g$  phonon, and vice versa. This coupling leads to the observed helicity reversal, where the  $E_g$  mode inherits the opposite helicity of the  $E_u$  phonon.

## Acknowledgments

We thank Michael Fechner, Hiroki Ueda, Prakriti P. Joshi, Alexander Paarmann for fruitful and friendly discussions. S.F.M. acknowledges support and funding from the Deutsche Forschungsgemeinschaft (DFG, grant No. 469405347) for his Emmy

Noether group “Circular Phononics”. D.M.J. acknowledges support from the Israel Science Foundation (ISF) Grant No. 1077/23 and 1916/23. D.M.J. further acknowledges support from the ERC Starting Grant CHIRALPHONONICS, no. 101166037.

## References

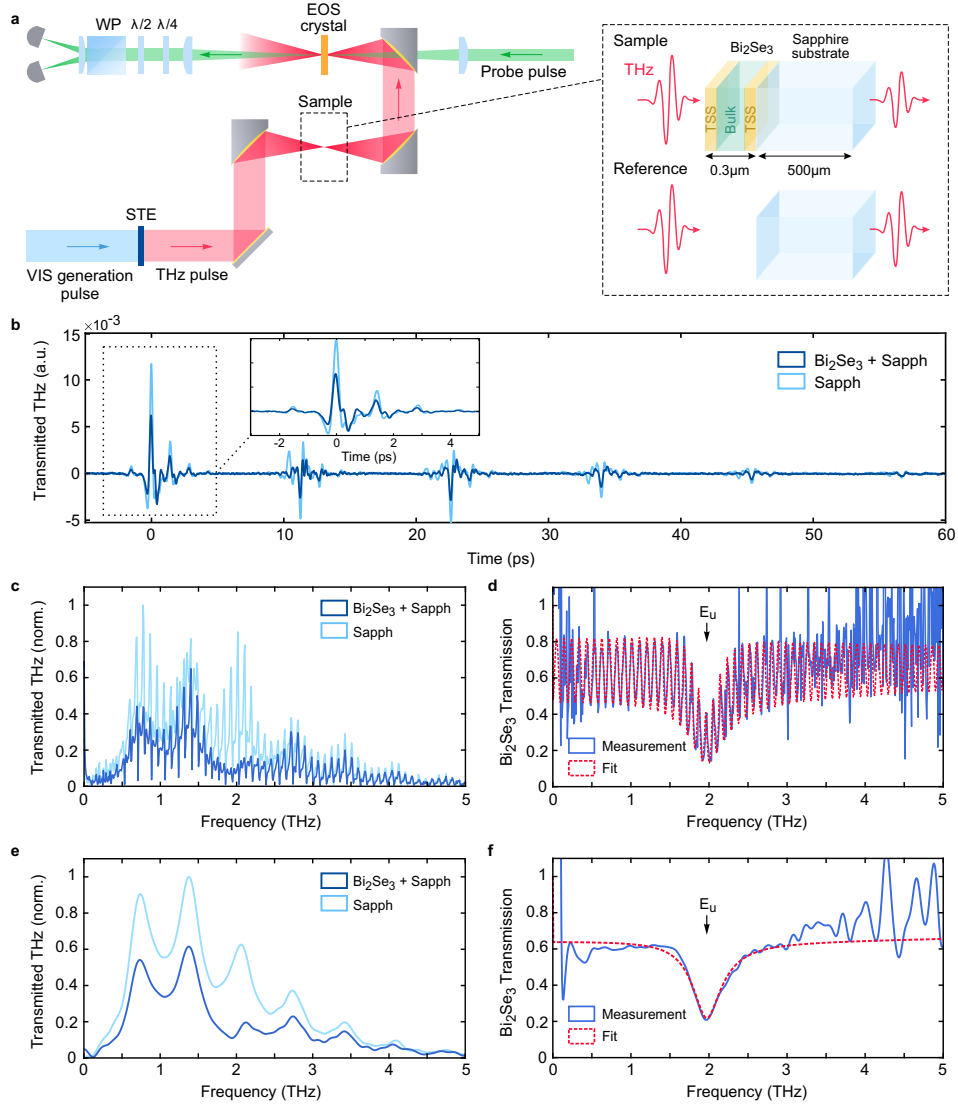
- [1] Zhu, H. *et al.* Observation of chiral phonons. *Science* **359**, 579 (2018). URL <http://science.sciencemag.org/content/359/6375/579.abstract>.
- [2] Ishito, K. *et al.* Truly chiral phonons in  $\alpha$ -hgs. *Nature Physics* (2022). URL <https://doi.org/10.1038/s41567-022-01790-x>.
- [3] Ueda, H. *et al.* Chiral phonons in quartz probed by X-rays. *Nature* **618**, 946–950 (2023). URL <https://www.nature.com/articles/s41586-023-06016-5>.
- [4] Luo, J. *et al.* Large effective magnetic fields from chiral phonons in rare-earth halides. *Science* **382**, 698–702 (2023). URL <https://www.science.org/doi/10.1126/science.adi9601>.
- [5] Grissonnanche, G. *et al.* Giant thermal Hall conductivity in the pseudogap phase of cuprate superconductors. *Nature* **571**, 376–380 (2019). URL <https://www.nature.com/articles/s41586-019-1375-0>.
- [6] Basini, M. *et al.* Terahertz electric-field-driven dynamical multiferroicity in SrTiO<sub>3</sub>. *Nature* **628**, 534–539 (2024). URL <https://www.nature.com/articles/s41586-024-07175-9>.
- [7] Choi, I. H. *et al.* Real-time dynamics of angular momentum transfer from spin to acoustic chiral phonon in oxide heterostructures. *Nature Nanotechnology* **19**, 1277–1282 (2024). URL <https://www.nature.com/articles/s41565-024-01719-w>.
- [8] Tauchert, S. R. *et al.* Polarized phonons carry angular momentum in ultrafast demagnetization. *Nature* **602**, 73–77 (2022). URL <https://doi.org/10.1038/s41586-021-04306-4>.
- [9] Davies, C. S. *et al.* Phononic switching of magnetization by the ultrafast Barnett effect. *Nature* **628**, 540–544 (2024). URL <https://www.nature.com/articles/s41586-024-07200-x>.
- [10] Einstein, A. & de Haas, W. J. Experimenteller nachweis der ampèreschen molekularströme. *Verh. Dtsch. Phys. Ges.* **17**, 152 (1915).
- [11] Dornes, C. *et al.* The ultrafast einstein-de haas effect. *Nature* **565**, 209–212 (2019). URL <https://doi.org/10.1038/s41586-018-0822-7>.
- [12] Orbach, R. . & Bleaney, B. Spin-lattice relaxation in rare-earth salts. *Proceedings of the Royal Society of London. Series A. Mathematical and Physical Sciences*

- 264, 458–484 (1997). URL <https://royalsocietypublishing.org/doi/abs/10.1098/rspa.1961.0211>.
- [13] Zhang, L. & Niu, Q. Angular momentum of phonons and the einstein–de haas effect. *PRL* **112**, 085503 (2014). URL <https://link.aps.org/doi/10.1103/PhysRevLett.112.085503>.
- [14] Teitelbaum, S. W. *et al.* Direct measurement of anharmonic decay channels of a coherent phonon. *PRL* **121**, 125901 (2018). URL <https://link.aps.org/doi/10.1103/PhysRevLett.121.125901>.
- [15] Garanin, D. A. & Chudnovsky, E. M. Angular momentum in spin-phonon processes. *PRB* **92**, 024421 (2015). URL <https://link.aps.org/doi/10.1103/PhysRevB.92.024421>.
- [16] Fausti, D. *et al.* Light-induced superconductivity in a stripe-ordered cuprate. *Science* **331**, 189–191 (2011). URL <http://www.sciencemag.org/content/331/6014/189.abstract>.
- [17] Mitrano, M. *et al.* Possible light-induced superconductivity in k3c60 at high temperature. *Nature* **530**, 461 (2016). URL <http://dx.doi.org/10.1038/nature16522>.
- [18] Fava, S. *et al.* Magnetic field expulsion in optically driven YBa2Cu3O6.48. *Nature* **632**, 75–80 (2024). URL <https://www.nature.com/articles/s41586-024-07635-2>.
- [19] Disa, A. S. *et al.* Photo-induced high-temperature ferromagnetism in YTiO3. *Nature* **617**, 73–78 (2023). URL <https://www.nature.com/articles/s41586-023-05853-8>.
- [20] Afanasiev, D. *et al.* Ultrafast control of magnetic interactions via light-driven phonons. *Nature Materials* (2021). URL <https://doi.org/10.1038/s41563-021-00922-7>.
- [21] Li, X. *et al.* Terahertz field-induced ferroelectricity in quantum paraelectric srtio3. *Science* **364**, 1079 (2019). URL <http://science.sciencemag.org/content/364/6445/1079.abstract>.
- [22] Juraschek, D. M. *et al.* Chiral phonons - perspective. *under review* (2025).
- [23] Juraschek, D. M., Fechner, M., Balatsky, A. V. & Spaldin, N. A. Dynamical multiferroicity. *Phys. Rev. Materials* **1**, 014401 (2017). URL <https://link.aps.org/doi/10.1103/PhysRevMaterials.1.014401>.
- [24] Nova, T. F., Disa, A. S., Fechner, M. & Cavalleri, A. Metastable ferroelectricity in optically strained srtio3. *Science* **364**, 1075 (2019). URL <http://science.sciencemag.org/content/364/6445/1075.abstract>.

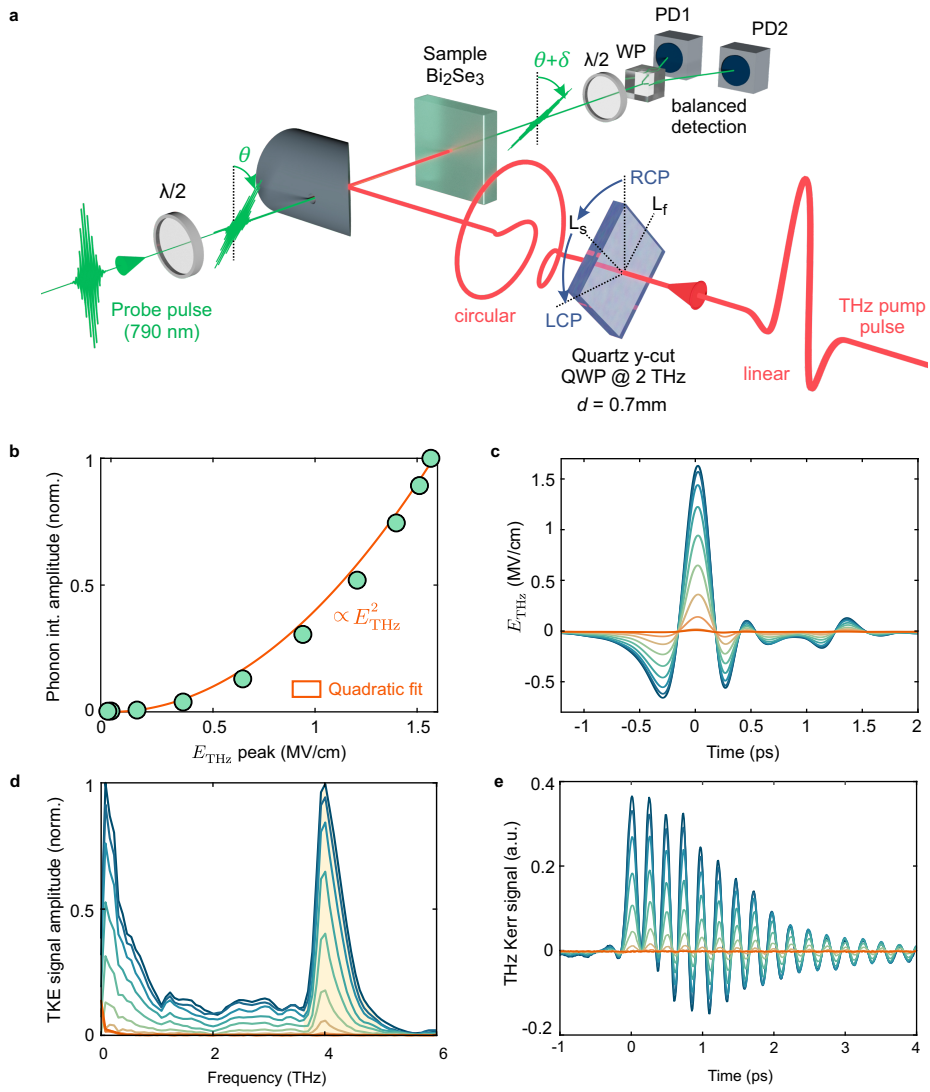
- [25] Juraschek, D. M., Neuman, T. & Narang, P. Giant effective magnetic fields from optically driven chiral phonons in  $\text{4f}$  paramagnets. *Physical Review Research* **4**, 013129 (2022). URL <https://link.aps.org/doi/10.1103/PhysRevResearch.4.013129>.
- [26] Merlin, R. Unraveling the effect of circularly polarized light on reciprocal media: Breaking time reversal symmetry with non-Maxwellian magnetic-esque fields. *Physical Review B* **110**, 094312 (2024). URL <https://link.aps.org/doi/10.1103/PhysRevB.110.094312>.
- [27] Wefers, M. M., Kawashima, H. & Nelson, K. A. Optical control over two-dimensional lattice vibrational trajectories in crystalline quartz. *The Journal of Chemical Physics* **108**, 10248–10255 (1998). URL <https://doi.org/10.1063/1.476485>.
- [28] Barnett, S. J. Magnetization by rotation. *PR* **6**, 239–270 (1915). URL <https://link.aps.org/doi/10.1103/PhysRev.6.239>.
- [29] Melnikov, A. A. *et al.* Coherent phonons in a  $\text{bi}_2\text{se}_3$  film generated by an intense single-cycle thz pulse. *PRB* **97**, 214304 (2018). URL <https://link.aps.org/doi/10.1103/PhysRevB.97.214304>.
- [30] Juraschek, D. M. & Maehrlein, S. F. Sum-frequency ionic raman scattering. *PRB* **97**, 174302 (2018). URL <https://link.aps.org/doi/10.1103/PhysRevB.97.174302>.
- [31] Blank, T. *et al.* Two-Dimensional Terahertz Spectroscopy of Nonlinear Phononics in the Topological Insulator  $\text{MnBi}_2\text{Te}_4$ . *Physical Review Letters* **131**, 026902 (2023). URL <https://link.aps.org/doi/10.1103/PhysRevLett.131.026902>.
- [32] Frenzel, M. *et al.* Nonlinear terahertz control of the lead halide perovskite lattice. *Science Advances* **9**, eadg3856 (2023). URL <https://www.science.org/doi/full/10.1126/sciadv.adg3856>.
- [33] Urban, J. M. *et al.* Thz-driven coherent phonon fingerprints of hidden symmetry breaking in 2d layered hybrid perovskites. *arXiv eprint* (2025). URL <https://arxiv.org/abs/2503.02529>.
- [34] Bloembergen, N. Conservation laws in nonlinear optics\*. *J. Opt. Soc. Am.* **70**, 1429–1436 (1980). URL <https://opg.optica.org/abstract.cfm?URI=josa-70-12-1429>.
- [35] Maehrlein, S., Paarmann, A., Wolf, M. & Kampfrath, T. Terahertz sum-frequency excitation of a raman-active phonon. *Phys. Rev. Lett.* **119**, 127402 (2017). URL <https://link.aps.org/doi/10.1103/PhysRevLett.119.127402>.

- [36] Richter, W. & Becker, C. R. A Raman and far-infrared investigation of phonons in the rhombohedral V2-VI3 compounds Bi2Te3, Bi2Se3, Sb2Te3 and Bi2(Te1-Se)3 ( $0 < x < 1$ ), (Bi1-Sb)2Te3 ( $0 < y < 1$ ). *physica status solidi (b)* **84**, 619–628 (1977). URL <https://onlinelibrary.wiley.com/doi/abs/10.1002/pssb.2220840226>.
- [37] Frenzel, M. *et al.* Quartz as an accurate high-field low-cost THz helicity detector. *Optica* **11**, 362–370 (2024). URL <https://opg.optica.org/optica/abstract.cfm?uri=optica-11-3-362>.
- [38] Johnson, C. L., Knighton, B. E. & Johnson, J. A. Distinguishing nonlinear terahertz excitation pathways with two-dimensional spectroscopy. *PRL* **122**, 073901 (2019). URL <https://link.aps.org/doi/10.1103/PhysRevLett.122.073901>.
- [39] Zhang, L. & Niu, Q. Chiral phonons at high-symmetry points in monolayer hexagonal lattices. *PRL* **115**, 115502 (2015). URL <https://link.aps.org/doi/10.1103/PhysRevLett.115.115502>.
- [40] Zahn, D. *et al.* Lattice dynamics and ultrafast energy flow between electrons, spins, and phonons in a 3d ferromagnet. *Physical Review Research* **3**, 023032 (2021). URL <https://link.aps.org/doi/10.1103/PhysRevResearch.3.023032>.
- [41] Stern, M. J. *et al.* Mapping momentum-dependent electron-phonon coupling and nonequilibrium phonon dynamics with ultrafast electron diffuse scattering. *PRB* **97**, 165416 (2018). URL <https://link.aps.org/doi/10.1103/PhysRevB.97.165416>.
- [42] Braun, L. *et al.* Ultrafast photocurrents at the surface of the three-dimensional topological insulator Bi2Se3. *Nature Communications* **7**, 13259 (2016). URL <https://www.nature.com/articles/ncomms13259>.
- [43] Sie, E. J. *et al.* An ultrafast symmetry switch in a weyl semimetal. *Nature* **565**, 61–66 (2019). URL <https://doi.org/10.1038/s41586-018-0809-4>.
- [44] Kittel, C. *Introduction to Solid State Physics* 8 th edn (John Wiley & Sons, Inc., New York, 2005).
- [45] Hübener, H., De Giovannini, U. & Rubio, A. Phonon Driven Floquet Matter. *Nano Letters* **18**, 1535–1542 (2018). URL <https://doi.org/10.1021/acs.nanolett.7b05391>.
- [46] Xu, Y. *et al.* Catalog of topological phonon materials. *Science* **384**, eadf8458 (2024). URL <https://doi.org/10.1126/science.adf8458>.
- [47] Gao, L., Prokhorenko, S., Nahas, Y. & Bellaïche, L. Dynamical Multiferroicity and Magnetic Topological Structures Induced by the Orbital Angular Momentum of Light in a Nonmagnetic Material. *Physical Review Letters* **131**, 196801 (2023). URL <https://link.aps.org/doi/10.1103/PhysRevLett.131.196801>.

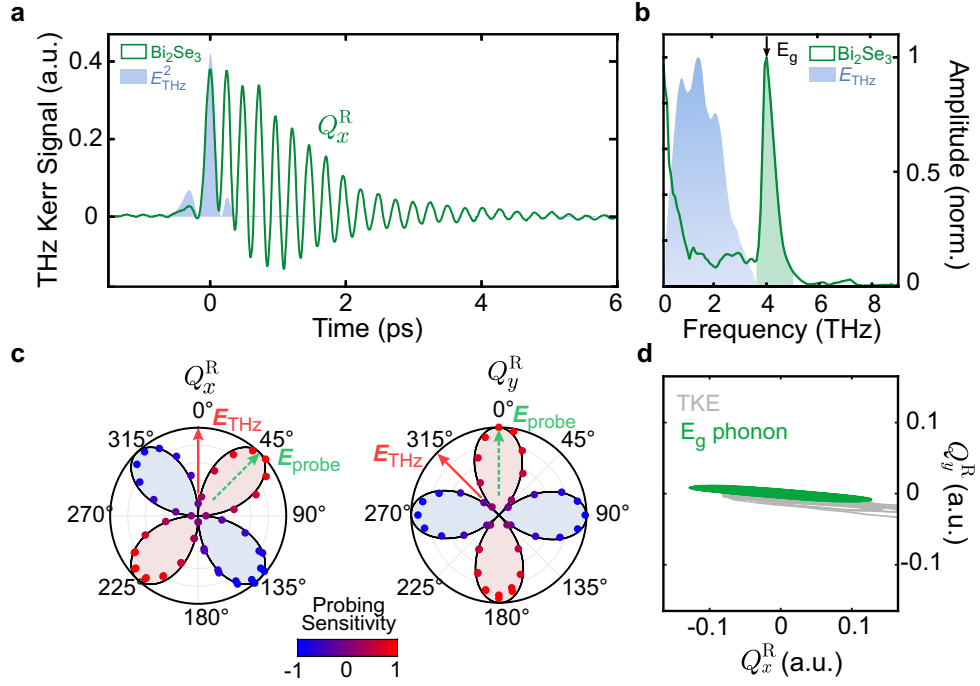
- [48] Hirori, H., Doi, A., Blanchard, F. & Tanaka, K. Single-cycle terahertz pulses with amplitudes exceeding 1 mv/cm generated by optical rectification in linbo<sub>3</sub>. *Appl. Phys. Lett.* **98**, 091106–3 (2011). URL <http://dx.doi.org/10.1063/1.3560062>.
- [49] Hoffmann, M. C., Brandt, N. C., Hwang, H. Y., Yeh, K.-L. & Nelson, K. A. Terahertz kerr effect. *Appl. Phys. Lett.* **95**, 231105 (2009). URL <http://dx.doi.org/10.1063/1.3271520>.
- [50] Rouzegar, R. *et al.* Broadband Spintronic Terahertz Source with Peak Electric Fields Exceeding 1.5 MV/cm. *Physical Review Applied* **19**, 034018 (2023). URL <https://link.aps.org/doi/10.1103/PhysRevApplied.19.034018>.
- [51] Loudon, R. The raman effect in crystals. *Advances in Physics* **13**, 423–482 (1964). URL <http://adsabs.harvard.edu/abs/1964AdPhy..13..423L>.



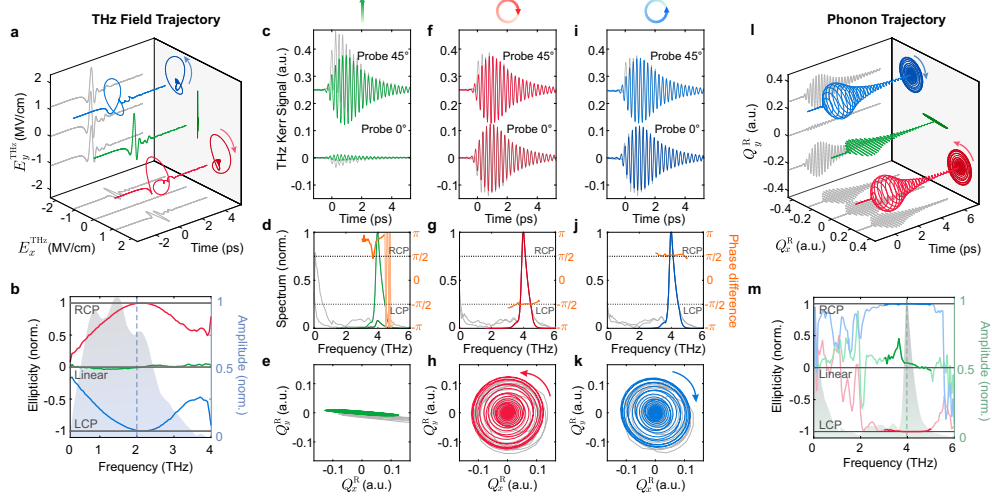
**Extended Data Fig. 1 Terahertz time-domain spectroscopy in  $\text{Bi}_2\text{Se}_3$**  **a**, Schematic of the THz transmission setup. An ultrabroadband THz pulse from a large-area spintronic emitter is focused onto the sample position at the first focal point. The transmitted field is then refocused onto a 30  $\mu\text{m}$ -thick GaP crystal for electro-optic detection. The sample position hosts either a 0.3  $\mu\text{m}$ -thick  $\text{Bi}_2\text{Se}_3$  film on a 500  $\mu\text{m}$  sapphire substrate or a bare 500  $\mu\text{m}$ -thick sapphire wafer for reference measurement. **b-c**, Time-domain signals of the sample (dark blue) and reference (light blue) THz transmission measurement, along with their corresponding Fourier transforms. **d**, Division of the THz spectrum transmitted through the sample (panel c, dark blue) by the reference spectrum (panel c, light blue), revealing the THz transmission of  $\text{Bi}_2\text{Se}_3$  and the absorption feature of the  $E_u$  phonon mode. The modeled  $\text{Bi}_2\text{Se}_3$  transmission function is shown as a red line, demonstrating very good correspondence. **e**, Fourier transforms of the fundamental transmitted pulse obtained by applying a 8 ps-time window to b. **f**, Corresponding ratio of transmitted THz spectra, as in d. Isolation of the fundamental transmitted pulses removes Fabry-Pérot oscillations from the transmission spectrum, enabling more precise modeling of the  $E_u$  phonon feature.



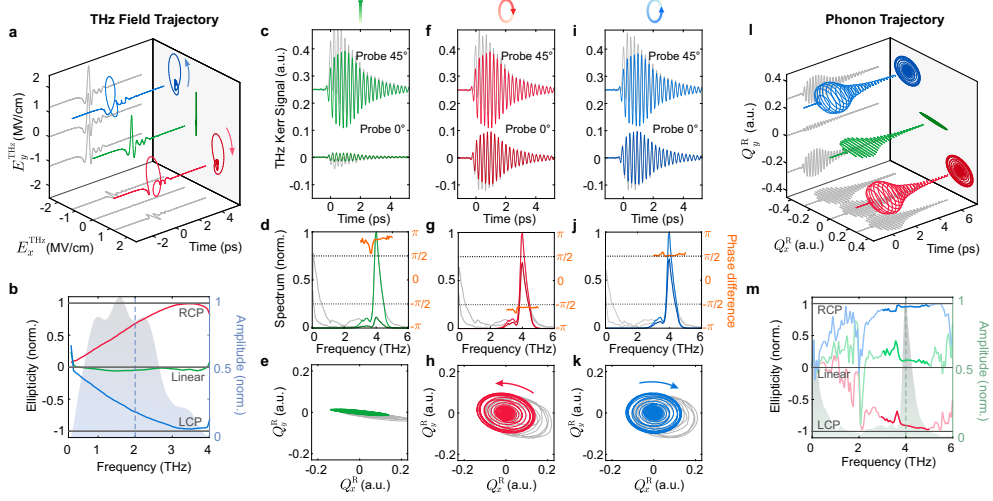
**Extended Data Fig. 2 Experimental TKE setup and THz field dependence a**, Schematic of the experimental TKE setup. A THz pulse, generated via optical rectification in  $\text{LiNbO}_3$ , passes through a 0.7mm-thick y-cut quartz waveplate to acquire a defined ellipticity state before irradiating the sample at normal incidence. The excited Raman-active phonon is detected via transient birefringence, which induces a time-dependent rotation of the probe pulse polarization, which is measured by a balanced detection. The angle of the incident probe pulse's linear polarization is controlled by a half-wave plate. **b-e**, THz fluence dependence of Raman-active  $E_g$  phonon. **b**, Integrated spectral amplitudes of the  $E_g$  mode as a function of THz peak electric field (purple points) with a corresponding quadratic fit (orange). **c**, Electro-optic sampling of incident THz fields. **d-e**, Corresponding TKE signals of  $\text{Bi}_2\text{Se}_3$  in frequency and time domain, respectively. The shaded area in **d** highlights the integration region used to determine the phonon amplitude.



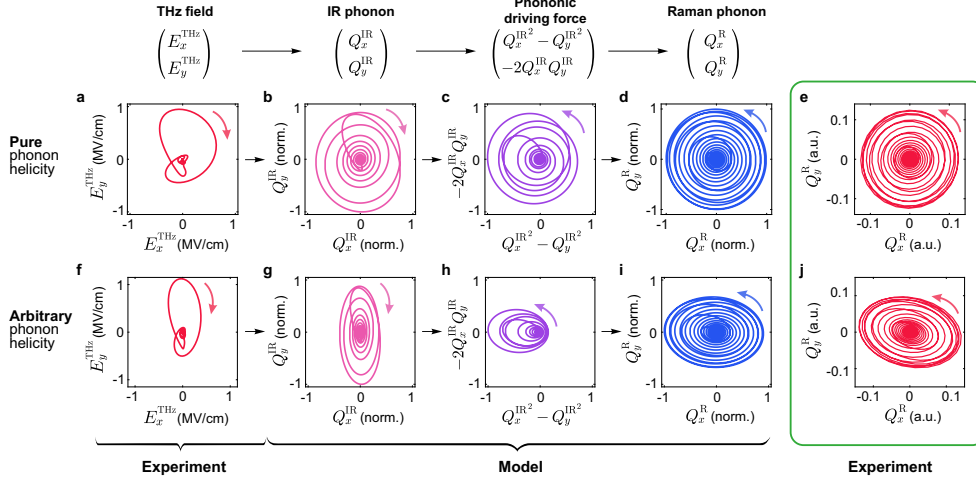
**Extended Data Fig. 3 Probing phonon trajectories** **a**, Measured THz-induced Kerr effect (TKE) in Bi<sub>2</sub>Se<sub>3</sub> (green) excited by a linearly polarized THz field pulse. The probe pulse is polarized at an angle of 45° relative to the THz excitation pulse. The TKE signal around time zero includes electronic contributions following  $E_{\text{THz}}^2$ . **b**, Fourier transforms of **a** unveils the prominent  $E_g$  phonon peak at 4 THz. **c**, Spectrally-integrated 4 THz coherent phonon amplitude (points) as a function of probe polarization angle (green arrow) relative to vertical and 45°-rotated THz excitation polarizations (red arrow), which drive orthogonal  $E_g$  phonon polarizations. The theoretically calculated TKE amplitude and the positive/negative sign are shown by the black line and shaded red/blue areas, respectively. **d**, Phonon trajectory of the linearly polarized  $E_g$  phonon measured with probe polarizations at 0° (y-component) and 45° (x-component). The gray line represents the entire TKE signal, while the green line shows the Fourier-filtered signal of the coherent phonon.



**Extended Data Fig. 4** Lattice trajectory control by circular THz excitation in  $\text{Bi}_2\text{Se}_3$ . **a**, Polarization-resolved EOS of the incident THz electric field transmitted through 700  $\mu\text{m}$ -thick y-cut quartz at three azimuthal crystal orientations. **b**, Frequency-resolved helicity states of the THz fields in **a**. The shaded grey area represents the THz spectral amplitude. **c-k**, Measured  $E_g$  trajectories under linear (green), right-circular (red) and left-circular (blue) THz excitation in  $\text{Bi}_2\text{Se}_3$ . **c**, Full TKE signals (grey) and Fourier-filtered phonon contributions (green) measured with probe polarized at  $0^\circ$  ( $S_{0^\circ}$ ) and  $45^\circ$  ( $S_{45^\circ}$ ), vertically offset for clarity, corresponding to two orthogonal  $E_g$  phonon components. **d**, Spectral amplitudes of signals in **c**, with the relative phase difference of the TKE signals  $S_{45^\circ} - S_{0^\circ}$  (orange). **e**, Corresponding vectoral phonon trajectory. **f-k**, Same data set as **c-e**, but for right- and left-circular THz excitation. **l**, Coherent phonon trajectories for each THz helicity (**a**), extracted by Fourier-filtering the phonon contribution in the TKE signal. **m**, Frequency-resolved helicity of the  $E_g$  phonon from **l**. The grey background represents the TKE spectrum, with the peak at 4 THz, corresponding to the Raman-active  $E_g$  phonon.



**Extended Data Fig. 5 Lattice trajectory control by arbitrary elliptical THz excitation in  $\text{Bi}_2\text{Se}_3$ .** **a**, Polarization-resolved EOS of the incident THz electric field transmitted through 380  $\mu\text{m}$ -thick y-cut quartz at three azimuthal crystal orientations. **b**, Frequency-resolved helicity states of the THz fields in **a**. The shaded grey area represents the THz spectral amplitude. **c-k**, Measured  $E_g$  trajectories under linear (green), right- (red) and left-handed (blue) elliptical THz excitation in  $\text{Bi}_2\text{Se}_3$ . **c**, Full TKE signals (grey) and Fourier-filtered phonon contributions (green) measured with probe polarized at  $0^\circ$  ( $S_{0^\circ}$ ) and  $45^\circ$  ( $S_{45^\circ}$ ), vertically offset for clarity, corresponding to two orthogonal  $E_g$  phonon components. **d**, Spectral amplitudes of signals in **c**, with the relative phase difference of the TKE signals  $S_{45^\circ} - S_{0^\circ}$  (orange). **e**, Corresponding vectoral phonon trajectory. **f-k**, Same data set as **c-e**, but for right- and left-handed elliptical THz excitation. **l**, Coherent phonon trajectories for each THz helicity state (**a**), extracted by Fourier-filtering the phonon contribution in the TKE signal. **m**, Frequency-resolved helicity of the  $E_g$  phonon from **l**. The grey background represents the TKE amplitude, with the peak at 4 THz, corresponding to the  $E_g$  phonon.



**Extended Data Fig. 6 Modeling the phonon trajectory in a classical picture.** **a-d, f-i,** Step-by-step modeling of the  $E_g$  phonon trajectory for purely circular (above) and arbitrary elliptical (below) THz excitation field. **a,** Vectorial trajectory of the right-handed circularly polarized THz electric field, measured by polarization-resolved EOS (Fig. 2a). The arrow indicates the direction of rotation. **b,** Corresponding IR-active  $E_u$  phonon trajectory, calculated by solving the equation of motion with the driving force set by the experimental THz pulse  $F_i^{\text{IR}}(t) = E_i^{\text{THz}}(t) - \partial V / \partial Q_i^{\text{IR}}, i \in \{x, y\}$ . **c,** Phononic driving force acting on the Raman-active  $E_g$  phonon, derived from the symmetry-allowed anharmonic coupling potential  $V(Q^{\text{IR}}, Q^{\text{R}}) = c(Q_x^{\text{IR}2} - Q_y^{\text{IR}2})Q_x^{\text{R}} - 2cQ_x^{\text{IR}}Q_y^{\text{IR}}Q_y^{\text{R}}$  between  $E_u$  and  $E_g$  modes. The driving force exhibits opposite helicity to the IR phonon in **b**. **d,** Calculated axial trajectory of Raman-active  $E_g$  phonon. **e,** Experimentally-retrieved  $E_g$  phonon trajectory, repeated from Fig. 2e. **f-j,** Same modeling procedure for arbitrary elliptically-polarized THz excitation (Extended Data Fig. 5a), with comparison to the experiment (Extended Data Fig. 5h).

# Supplementary Information

## S1. Analytical Model for THz Transmission of Bi<sub>2</sub>Se<sub>3</sub>

To analyze the THz transmission of Bi<sub>2</sub>Se<sub>3</sub> and determine the phonon lifetime of the E<sub>u</sub> mode  $\tau_{\text{IR}}$ , we derive the analytical expression based on Fresnel coefficients. The analytical solution accounts for all internal reflections within both the Bi<sub>2</sub>Se<sub>3</sub> sample and the sapphire substrate. Owing to the topological insulating properties of Bi<sub>2</sub>Se<sub>3</sub>, the material is represented as a three-layer system comprising an insulating bulk sandwiched between two conductive topological surface states (TSS). Figure S4 illustrates the layered structure and defines the associated transmission and reflection coefficients. The multilayer stack consists of a TSS ( $n_1$ , refractive index), a Bi<sub>2</sub>Se<sub>3</sub> bulk layer ( $n_2$ , refractive index), a TSS ( $n_1$ , refractive index), and a sapphire substrate ( $n_3$ , refractive index), surrounded by air ( $n_0$ , refractive index) from both sides. The THz pulse propagates at normal incidence through the layers in the sequence  $n_0 \rightarrow n_1 \rightarrow n_2 \rightarrow n_1 \rightarrow n_3 \rightarrow n_0$ .

The reference transmission function for sapphire,  $T_{\text{sapph}}(\omega)$ , is derived for a single layer, accounting for multiple beam interference within the substrate:

$$T_{\text{sapph}}(\omega) = \frac{t_{03}t_{30}e^{i\varphi_3}}{1 - r_{30}^2e^{i2\varphi_3}}. \quad (\text{S1})$$

Here,  $t_{ij}(\omega)$  and  $r_{ij}(\omega)$  denote the Fresnel transmission and reflection coefficients for a wave propagating from media  $i$  and  $j$ , defined as  $t_{ij}(\omega) = 2n_i/(n_i + n_j)$  and  $r_{ij}(\omega) = (n_i - n_j)/(n_i + n_j)$ . The phase  $\varphi_3$  accounts for the THz pulse propagation through the sapphire layer of thickness  $d_3 = 500 \mu\text{m}$ , given by  $\varphi_3(\omega) = (\omega n_3(\omega)d_3)/c_0$ , where  $c_0$  is the speed of light in vacuum.

To derive the transmission function  $T_{\text{total}}(\omega)$ , we employ an iterative approach that systematically reduces a multilayer system to an effective single-layer model by incorporating the contribution of other layers into the modified transmission and reflection coefficients at the interfaces. As the first step, the Bi<sub>2</sub>Se<sub>3</sub> sample is treated as an effective interface between air and the sapphire substrate, characterized by the transmission ( $T_{03}$ ) and reflection ( $R_{30}$ ) coefficients. This simplification reduces the system to an equivalent single-layer sapphire ( $n_3$ ) model, analogous to the reference case, so the THz transmission function through the sample and the substrate  $T_{\text{total}}(\omega)$  can be expressed as:

$$T_{\text{total}}(\omega) = \frac{T_{03}t_{30}e^{i\varphi_3}}{1 - r_{30}R_{30}e^{i2\varphi_3}}. \quad (\text{S2})$$

To determine  $T_{03}$  and  $R_{30}$ , we separately consider a three-layer Bi<sub>2</sub>Se<sub>3</sub> sample and reduce its complexity to a single layer-model of the bulk ( $n_2$ ) sandwiched between air ( $n_0$ ) and sapphire ( $n_3$ ), with effective interfaces defined by the TSSs (Fig. S4a). Here we introduce the transmission and reflection coefficients at the air-bulk ( $T_{02}$ ,  $R_{20}$ ), and bulk-sapphire ( $T_{23}$ ,  $R_{23}$ ,  $T_{32}$ ,  $R_{32}$ ) interfaces, so the transmission and reflection

of the  $\text{Bi}_2\text{Se}_3$  sample can be written as:

$$T_{03}(\omega) = \frac{T_{02}T_{23}e^{i\varphi_2}}{1 - R_{20}R_{23}e^{i2\varphi_2}}, \quad R_{30}(\omega) = R_{32} + \frac{T_{32}T_{23}R_{20}e^{i2\varphi_2}}{1 - R_{20}R_{23}e^{i2\varphi_2}}, \quad (\text{S3})$$

where  $\varphi_2(\omega) = (\omega n_2(\omega)d_2)/c_0$  stands for the phase accumulated by the THz pulse propagating through the  $\text{Bi}_2\text{Se}_3$  bulk with a thickness of  $d_2 = 0.3 \mu\text{m}$ . The frequency-dependent coefficients  $T_{02}(\omega)$ ,  $R_{20}(\omega)$  and  $T_{23}(\omega)$ ,  $R_{23}(\omega)$ ,  $T_{32}(\omega)$ ,  $R_{32}(\omega)$  are explicitly derived by considering two TSS layers independently: one interfacing with air and the bulk, and the other with the bulk and sapphire (see Fig. S4b,c). These coefficients can be expressed in term of the Fresnel coefficients as follows:

$$T_{02}(\omega) = \frac{t_{01}t_{12}e^{i\varphi_1}}{1 - r_{10}r_{12}e^{i2\varphi_1}}, \quad R_{20}(\omega) = r_{21} + \frac{t_{21}t_{12}r_{10}e^{i2\varphi_1}}{1 - r_{10}r_{12}e^{i2\varphi_1}}, \quad (\text{S4})$$

$$T_{23}(\omega) = \frac{t_{21}t_{13}e^{i\varphi_1}}{1 - r_{13}r_{12}e^{i2\varphi_1}}, \quad R_{23}(\omega) = r_{21} + \frac{t_{21}t_{12}r_{13}e^{i2\varphi_1}}{1 - r_{13}r_{12}e^{i2\varphi_1}}, \quad (\text{S5})$$

$$T_{32}(\omega) = \frac{t_{31}t_{12}e^{i\varphi_1}}{1 - r_{13}r_{12}e^{i2\varphi_1}}, \quad R_{32}(\omega) = r_{31} + \frac{t_{31}t_{13}r_{12}e^{i2\varphi_1}}{1 - r_{13}r_{12}e^{i2\varphi_1}}, \quad (\text{S6})$$

where  $\varphi_1(\omega) = (\omega n_1(\omega)d_1)/c_0$  with  $d_1 = 1 \text{ nm}$ .

Therefore, using this iterative approach, we reduce the model's complexity and derive the THz transmission function  $T_{\text{total}}(\omega)$  in terms of only Fresnel coefficients and phase factors. The calculated THz transmission function of  $\text{Bi}_2\text{Se}_3$ , presented in Extended Data Fig. 1d, is determined by

$$T_{\text{Bi}_2\text{Se}_3}(\omega) = T_{\text{total}}(\omega)/T_{\text{sapph}}(\omega). \quad (\text{S7})$$

To model the  $\text{Bi}_2\text{Se}_3$  measured transmission function obtained from the windowed time-domain EOS traces (see Extended Data Fig. 1f), we keep only the contribution from the fundamental transmitted THz pulse by retaining only the numerators in  $T_{\text{total}}(\omega)$  and  $T_{\text{sapph}}(\omega)$ . The sample and substrate transmission functions therefore take the form

$$T_{\text{total}}(\omega) = T_{03}t_{30}e^{i\varphi_3}, \quad (\text{S8})$$

$$T_{\text{sapph}}(\omega) = t_{03}t_{30}e^{i\varphi_3}, \quad (\text{S9})$$

respectively, leading to the  $\text{Bi}_2\text{Se}_3$  transmission function  $T_{\text{Bi}_2\text{Se}_3}(\omega) = T_{03}(\omega)/t_{03}(\omega)$ .

The dielectric functions for the distinct layers of the  $\text{Bi}_2\text{Se}_3$  sample are defined using different models tailored to their properties. The Lorentz oscillator model is employed for the insulating  $\text{Bi}_2\text{Se}_3$  bulk  $\varepsilon_{\text{bulk}}(\omega)$ , while the Drude model is used for the conducting topological surface states  $\varepsilon_{\text{TSS}}(\omega)$ . The dielectric functions for air and sapphire are set as  $\varepsilon_{\text{air}}(\omega) = 1$  and  $\varepsilon_{\text{sapph}}(\omega) = 3$ . For the topological surface states, the dielectric function is given by

$$\varepsilon_{\text{TSS}}(\omega) = 1 - \frac{\omega_{\text{pl}}^2}{\omega^2 + i\gamma\omega}, \quad (\text{S10})$$

with  $\omega_{\text{pl}}=1050$  THz and  $\gamma = 20$  THz. The introduction of conducting TSS layers at the interfaces allows to capture the reduction in the THz transmission across the spectrum. For the  $\text{Bi}_2\text{Se}_3$  bulk, the dielectric function is set as

$$\varepsilon_{\text{bulk}}(\omega) = \varepsilon_{\infty} + \frac{S\omega_{\text{IR}}^2}{\omega_{\text{IR}}^2 - \omega^2 - i\gamma_{\text{IR}}\omega}, \quad (\text{S11})$$

with  $\varepsilon_{\infty} = 40$ ,  $S = 100.5$  THz,  $\omega_{\text{IR}} = 1.97$  THz and  $\gamma_{\text{IR}} = 0.20$  THz. The parameters  $\omega_{\text{IR}}$ ,  $\gamma_{\text{IR}}$ ,  $S$  are the frequency of IR-active  $E_u$  phonon, its damping rate and the oscillator strength, respectively. These parameters of the dielectric functions were adjusted to model the experimental data, focusing on determining the phonon frequency  $\omega_{\text{IR}}$  and phonon damping rate  $\gamma_{\text{IR}}$ . The  $E_u$  phonon life time is determined as  $\tau_{\text{IR}} = 1/\gamma_{\text{IR}}$  and equals 5 ps.

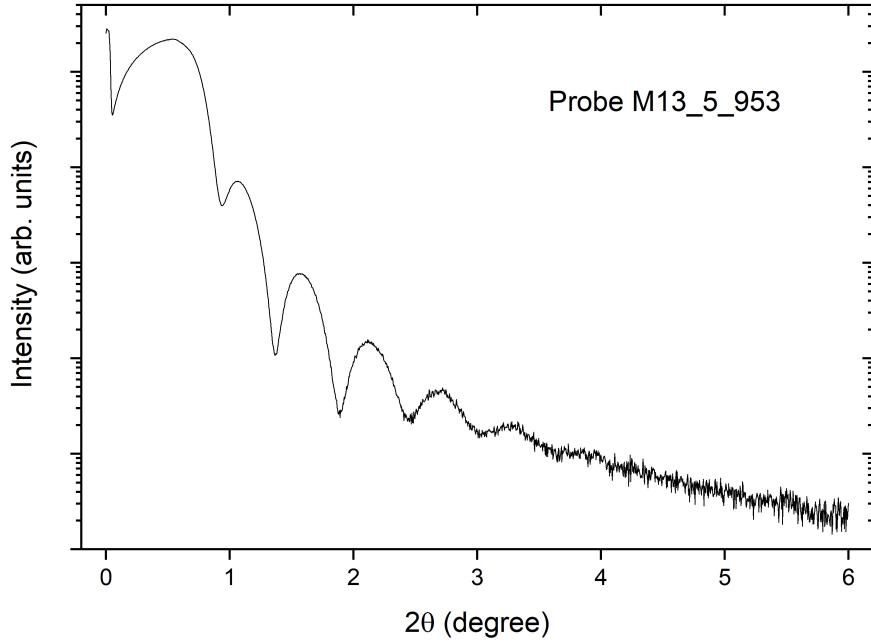


**Fig. S1 X-ray reflectivity (XRR).** XRR curve of the used  $\text{Bi}_2\text{Se}_3$  sample. From the periodicity of the oscillations, a  $\text{Bi}_2\text{Se}_3$  thickness  $d = 15.0$  nm is determined.

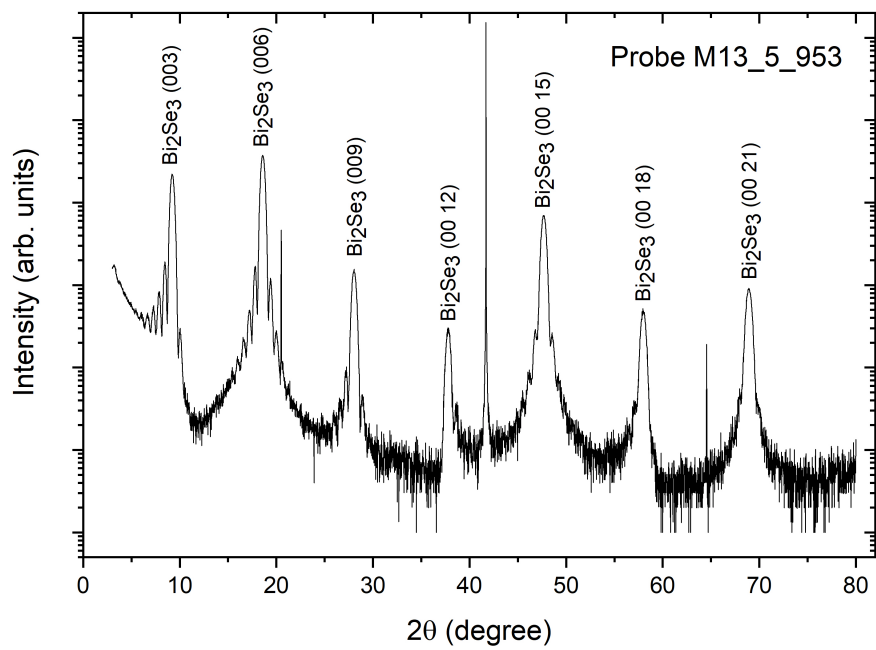


**Fig. S2 X-ray Diffraction (XRD).** Symmetric  $2\theta/\theta$  XRD curve of the investigated sample with numerous peaks from the epilayer, evidencing the correct  $\text{Bi}_2\text{Se}_3$  stoichiometry as well as the single-crystal nature of the  $\text{Bi}_2\text{Se}_3$  film.

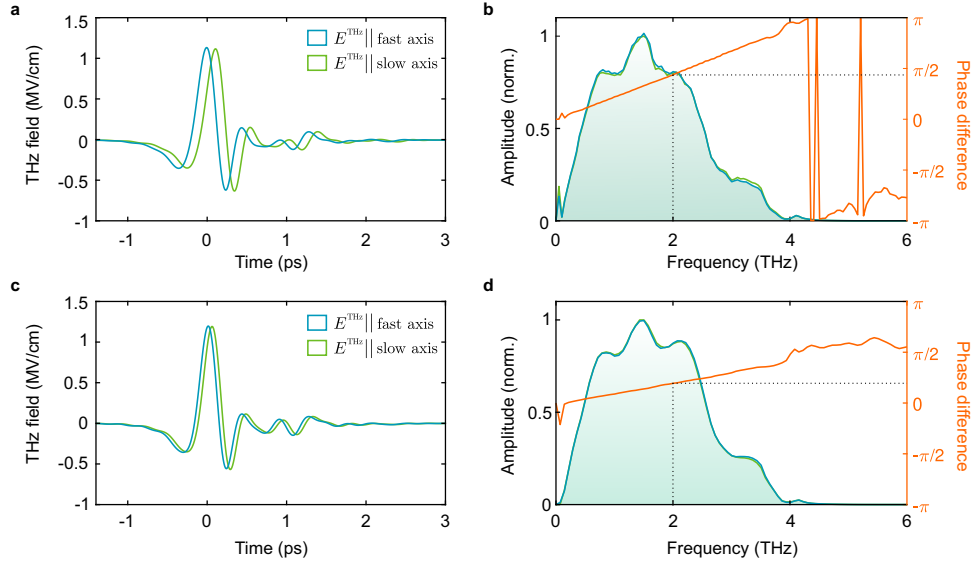


**Fig. S3 Characterization of the quartz waveplates.** **a**, Linearly-polarized THz electric fields after propagating through a 700  $\mu\text{m}$ -thick y-cut quartz waveplate, measured via electro-optic sampling in a 50  $\mu\text{m}$ -thick z-cut quartz detection crystal. Dark green and light green traces correspond to THz fields aligned with the fast and slow axes of y-cut quartz, respectively. **b**, Corresponding Fourier transforms of the THz fields and their relative phase difference (orange). At 2 THz, the phase difference is about  $\pi/2$ , indicating the generation of a circularly polarized THz pulse when the incident field is oriented at  $45^\circ$  to the fast and slow axes. **c-d**, Same measurements as a–b, but for a 380  $\mu\text{m}$ -thick y-cut quartz waveplate. The phase difference at 2 THz results in the generation of an arbitrarily elliptical THz polarization state when the incident THz field is oriented at  $45^\circ$  relative to the crystal axes.

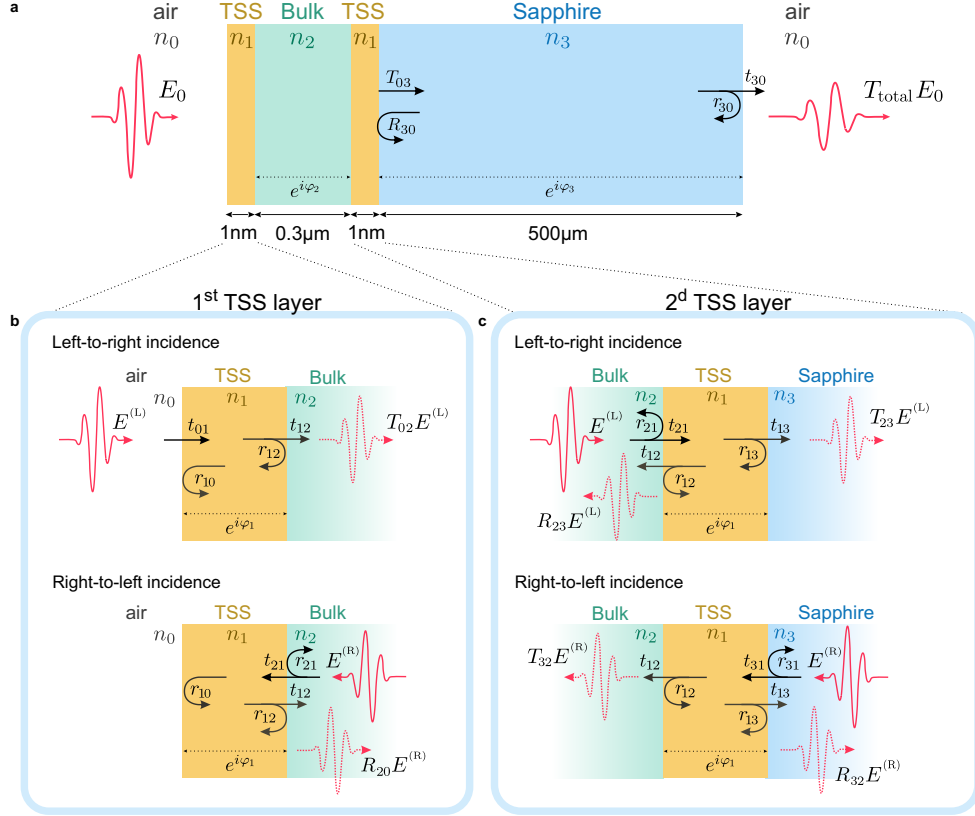


**Fig. S4 Multilayer thin-film interference model.** **a**, Schematic of multilayer system of  $\text{Bi}_2\text{Se}_3$  sample on the sapphire substrate and the transmitted THz field (red waveform).  $\text{Bi}_2\text{Se}_3$  is represented as a three-layer system of an insulating bulk layer sandwiched between two conductive surface layers (TSS). **b-c**, Transmission and reflection of the THz pulse from the first and second TSS layers, respectively.  $t_{ij}$  and  $r_{ij}$  are the Fresnel transmission and reflection coefficients for a wave propagating from medium  $i$  into medium  $j$ .  $T_{ij}$  and  $R_{ij}$  accounts for all internal reflections between the media  $i$  and  $j$ .